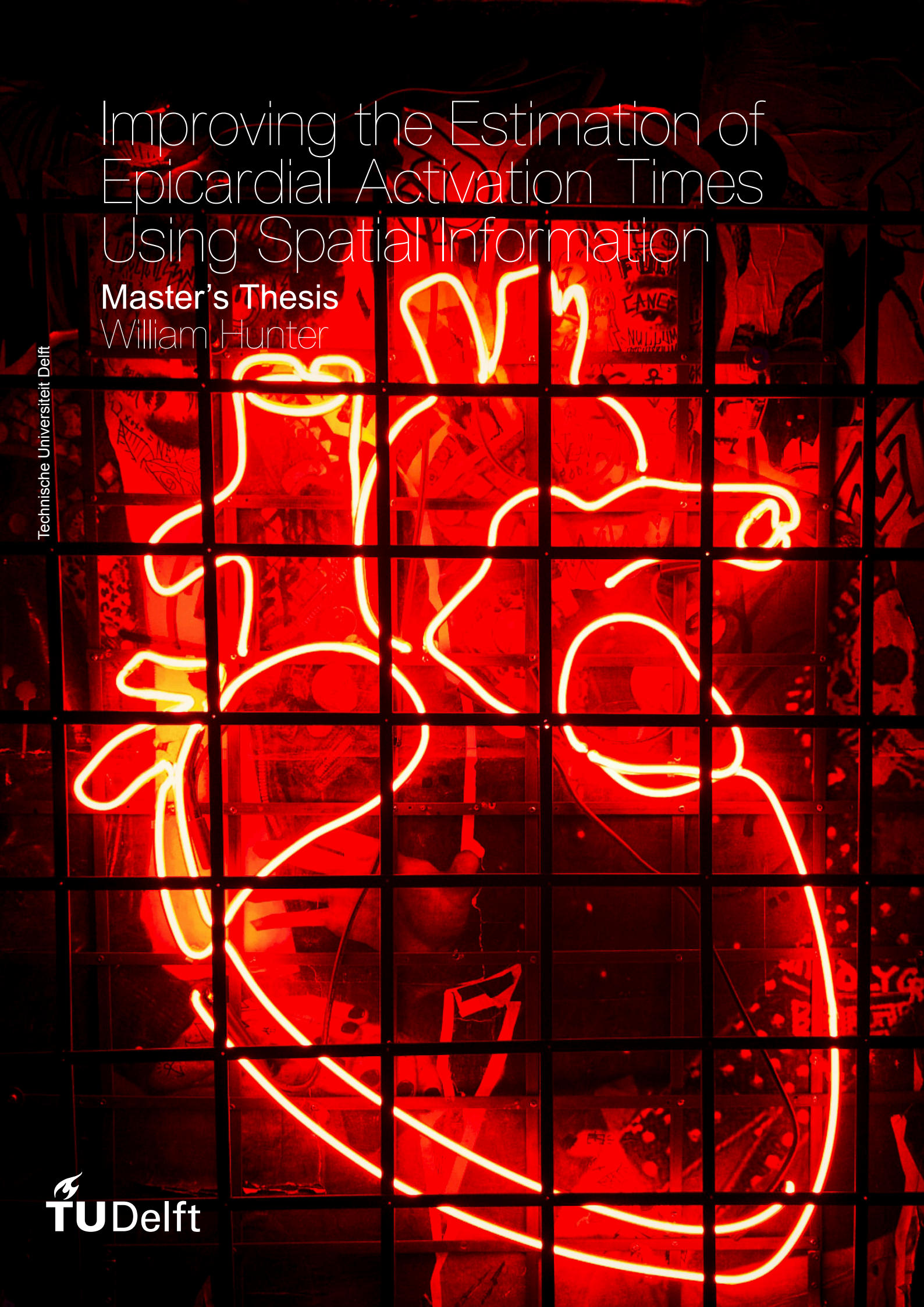

Improving the Estimation of Epicardial Activation Times Using Spatial Information

Master's Thesis

William Hunter

Technische Universiteit Delft

TU Delft

Improving the Estimation of Epicardial Activation Times Using Spatial Information

Thesis

by

A. W. G. Hunter BSc

submitted in partial fulfillment of the requirements for the degree of

Master of Science
in Electrical Engineering

at Delft University of Technology,
to be defended publicly on Monday August 29, 2022 at 9.30 AM.

Student number: 4478827
Project duration: April 20, 2021 – August 29, 2022
Thesis committee:

dr. ir. R. C. Hendriks,	Circuits and Systems, chairman
dr. C. M. Boutry,	Electronic Components, Technology and Materials
dr. B. Abdikivanani,	Electrical Engineering Education

An electronic version of this thesis is available at http://repository.tudelft.nl/.

TU Delft

This work was performed in:

Circuits and Systems Group
Department of Microelectronics
Faculty of Electrical Engineering, Mathematics and Computer Science
Delft University of Technology

Summary

Cardiovascular disease is the leading cause of death worldwide. As the average lifespan increases, its incidence and impact will only increase in the years to come, too. Atrial fibrillation is a common cardiovascular disease, affecting the regular beating of the heart through chaotic contraction of the heart's upper chambers. On its own, the condition—increasingly prevalent among the elderly—is not life threatening, but it leads to an increased risk of stroke and heart failure. As of yet, there is no consensus on the physiological mechanisms responsible for initiating and sustaining atrial fibrillation. A more detailed view of cardiac activity would improve understanding of the disease, making earlier diagnosis possible and improving options for treatment.

The contraction of the cardiac muscles is governed by electrical signals propagating through the tissue. This makes it possible to monitor cardiac activity by recording electrical signals on the heart. A high spatial resolution can be achieved by measuring the electrical potential directly on the epicardium of the heart during open-heart surgery using an array of closely spaced electrodes. From these electrograms, estimating the time of local activation of the cardiac tissue underneath each electrode provides a quantitative way of mapping the propagation of waves of contraction and getting a better sense of the mechanisms of atrial fibrillation.

Various methods exist to estimate the activation times, but the complex signals that are typical of atrial fibrillation make it difficult to obtain accurate results. This thesis proposes combining two existing methods for estimating the local activation times. As a first step, deconvolution is applied to the electrograms. Based on a model of the electrogram as a spatial convolution of local transmembrane currents, an inverse problem is formulated and solved in a regularized least-squares sense. The currents thus obtained give a less opaque view of the cardiac activity at the electrode locations by attenuating distant disturbances and emphasizing local activity. The deconvolution output is fed to the second step of cross-correlation over higher-order neighbors. Cross-correlating certain pairs of signals gives an estimate for the mutual time delay in local activation. A graph representation of the electrode array is used to define neighbor order and decide which signal pairs are correlated. The set of pairwise time delays this produces is then converted to an estimate for the local activation times, using a least-squares estimator.

The performance of the proposed method is evaluated using simulated data of atrial cardiac activity, producing simulated electrograms. To model different cardiac settings, three types of tissue conductivity patterns are used, along with the option to model multiple sources of electrical stimulation. Using a single-source setting, earlier results of the deconvolution and cross-correlation methods are confirmed, and the proposed method is seen to produce a slightly lower mean error than reference methods. In the higher-complexity triple-source setting, the latter effect is again visible. Reinforced by the performance of the different methods in increasingly noisy settings, the main merits of the proposed method for the estimation of local activation times can be said to be found in the form of increased consistency, not significantly improving on the accuracy of existing methods.

Preface

This thesis represents the concluding part of the Master's program in Electrical Engineering, in the track of Signals and Systems, submitted as the final deliverable for obtaining the title of Master of Science in Electrical Engineering, or *elektrotechnisch ingenieur* in Dutch, at the Faculty of Electrical Engineering, Mathematics and Computer Science. This makes me one of the many thousands to have reached this milestone since this field of study was introduced in Delft in 1905 [1]–[3]. A lot has changed since that time, when the discipline was treated here more as a subset of mechanical engineering. Electrical engineering later became a faculty in its own right and today, the world relies on this branch of knowledge more than ever. Electrical engineering has become an intrinsic, indispensable part of many other subjects. This effect is also embedded in this thesis, in which electrical-engineering know-how is applied to a topical problem in a medical setting.

The work described in this thesis, along with the efforts of other Master's and PhD students, is part of the Atrial Fibrillation Fingerprinting project, a collaboration between Delft University of Technology, Erasmus University Medical Center and VU University Medical Center. The goal of the project is to develop a better understanding of atrial fibrillation, its causes and manifestations. This will allow a more effective way of diagnosis to be set up, paving the way for optimal treatment of atrial fibrillation and improving the outcome of patients suffering from this disease.

There are quite a number of people I owe a debt of gratitude to in reaching this point. First of all, I want to thank the thesis committee for their time and interest in my work. Specifically, thanks go out to my supervisor, Richard, for asking critical questions, pointing out interesting research directions and keeping the project moving forward, and to my daily supervisor, Bahareh. Your work formed an important basis of this thesis and you were always ready to explain, answer questions and provide some perspective on the subject. I had the opportunity to attend your doctoral defense ceremony last fall, which provided a nice frame of reference for my own work.

Thanks to the students of the Circuits and Systems (CAS) group, the section under whose auspices my project fell. In particular, I would like to thank Ruben, Sebas, Mosab, Koen, and Edoardo, my roommates in the newly renovated CAS enclave on the 18th floor. From complaining about the blinds and enjoying the five-star view to discovering secret sources of coffee, your useful comments and fun distractions helped make the latter months of my project more stimulating.

Apart from these direct academic contacts, there are a number of other factors that made my years in Delft such an enjoyable experience. Over the course of my seven years in the *Prinsenstad*, the Electrotechnische Vereeniging (ETV) has offered me a lot. *De oude dame* provided me with my very first acquaintances here as well as close friends to this day, provided me with sufficient occasions for coffee breaks, gave me a great platform for personal development, and indulged my interest in the history of our faculty through her rich archives, all of which I am most grateful for. For the unforgettable year of 2017–2018 and many amazing moments since, I want to thank my fellow members of the 146th ETV Board. I give a special shout-out to Tijs: for a lot of the days I spent working on this project, you were my trusty companion, having started at approximately the same time as I did. I am grateful for all your support, as well as for you proofreading part of this document.

Fellow clients of Joey Travels, thanks for all the shared adventures, which took us from Rotterdam to South Africa and from Croatia to the French Alps, in varying circumstances. I would especially like to thank two fellow jesters: Bart, for providing another foundation for my work and taking the time to explain his findings to me; and the namesake of the earlier-mentioned up-and-coming travel agency, Joey, both for organizing the wonderful outings we have experienced together and for all the coffees he made possible.

I had the additional pleasure of being a member of Groover, which allowed me to surround myself with musicians, and which provided the perfect soundtrack to my time in Delft. I am continually happy to be a part of the Van Gasteren Quintet, which provided (and still provides) me with great opportunities to boost my musical knowledge and great memories to boot. Let me not forget the great gents from Sjoes, particularly Ingo, with whom I could share this journey of thesis writing (as well as the handy phrase *Deo volente*). You have been a source of great support over the years: thank you!

Last, but certainly not least, I want to thank my family. My parents and sisters have always supported me, in more ways than I could possibly mention here, helping me get to this point. The fact that you are reading this document is a testament to their unfailing encouragement and interest. Special thanks go out to my mother for proofreading this thesis: *baie dankie!*

Of course, it is only correct that I finally also thank you, the reader, for your interest in this thesis. Enjoy reading it!

A. W. G. Hunter BSc
Delft, August 2022

Contents

List of figures

List of tables

1 Introduction

1.1. Research motivation

The leading cause of death worldwide is cardiovascular disease (CVD). This wide class of diseases affecting the heart and blood vessels was responsible for the death of an estimated 17.9 million people in 2019, representing 32% of all global deaths in that year [4]. Apart from the direct impact through loss of life, CVD also places a heavy burden on society through its economic impact. In 2015, it was estimated that CVD cost the European Union economy €210 billion (made up of healthcare costs, loss of productivity, and informal care of people with CVD) [5]. This makes the total costs due to CVD more than those for any other diagnostic group [6]. In the European Union, the group of approximately 49 million people living with the disease is increasing by 6 million new cases every year [5].

Within the class of CVD, we can distinguish a group of diseases that affect the regular beating of the heart, known as cardiac arrhythmias. These conditions are becoming ever-prevalent in populations as people become older in general, as a result of which they have come to be referred to as “the cardiovascular epidemic of the 21st century” [7]. The most common cardiac arrhythmia is atrial fibrillation (AF), which manifests itself as disorganized contraction of the muscles in the upper chambers (atria) of the heart. As a result, the heart pumps blood around the body less efficiently, increasing the overall risk of mortality [8] and the risk of other complications, such as blood clots, stroke, and heart failure [9]. AF is widespread: in Europe, 1 to 3 percent of the population suffers from the condition, with the percentage being higher among the elderly [10]. As life expectancy increases, the occurrence of AF increases with it [11], with the number of cases expected to double by 2060 [10]. A large volume of research has been done into AF, resulting in some understanding of the mechanisms behind it. However, as of yet there is no global consensus on this matter [12], which is detrimental to the progress of finding effective forms of treatment.

A good understanding of cardiac activity and other processes in the heart starts with finding a method to register and quantify them. The rhythmic contraction of cardiac muscles is controlled by the coordinated conduction of electrical signals. As a result, the activity of the heart can be monitored by measuring its electrical activity. The first tools for visualizing and recording cardiac activity were developed at the end of the 19th century, and led to the introduction of the electrocardiogram (ECG) using the string galvanometer developed by Willem Einthoven [13], [14]. From this method, which involved attaching electrical leads to a patient’s limbs to measure the current, improvements and subsequent discoveries led to the 12-lead ECG method that is in common use today [15].

An ECG constitutes an effective way of gauging the total electrical activity of the heart. Different parts of the standard cardiac cycle can be identified and validated on ECG recordings, and AF is often first diagnosed using an ECG. However, this method, using electrodes applied to the skin, is less suited for obtaining specific information on local activity in sections of cardiac tissue. A solution to this problem can be found by measuring the electrical activity directly on the surface of the heart during open-heart surgery, using an array of electrodes. These invasive recordings, known as electrograms, offer a much finer spatial resolution [16].

Electrograms can contain a lot of information about the spatial progression of the electrical signals in the heart over time, allowing us to quantify the activity of the heart in a more detailed manner. From

each electrode used in the recording, a quantity of particular interest is the exact moment at which the section of tissue underneath that electrode is activated, which is known as the local activation time (LAT). Using this LAT from each electrode, the “path” of activation through heart tissue can be mapped, giving us a location-based view of how and where the cardiac muscle contracts over time. This mapping process can bring to light obstacles of the activation wave, such as blocks in electrical conduction or multiple interfering sources of electrical activity.

There are various methods for obtaining the LATs from measured electrograms. This can be done manually, with an expert physician reviewing the measured signals and hand-picking the moment of activation per electrode. Though it offers increased accuracy, this method is time and labor intensive. The LAT can also be determined using a variety of automated methods. The most commonly used technique is the steepest-deflection (SD) method [17], which consists of processing the electrograms by marking the moment at which the slope of the signal is at its steepest (i.e., obtains its maximally negative value) as the LAT. The accuracy of SD decreases as more complex signals are considered, such as can be encountered during AF [18].

Two other methods used in this context are deconvolution and cross-correlation. In contrast to SD, these methods employ the spatial information encoded in the array of measured signals. Similarly to how the ECG can be seen as the spatial average of activity of the whole heart, the deconvolution method views a single electrogram as the spatial average of cardiac activity in the neighborhood of the measuring electrode. It then seeks to process the electrogram in such a way as to obtain this underlying, “less blurry” image of cardiac activity [19]. Cross-correlation methods can be used to estimate the delay between two similar signals. From these pairwise delays, further processing can produce the LATs. This cross-correlation can be applied to neighboring electrodes [20], or to electrodes that are farther apart as well [21].

1.2. Research objectives

This thesis investigates the application of a combination of deconvolution and cross-correlation methods for the mapping of electrical activity in the atria. Specifically, we explore estimating the LATs from atrial electrograms using existing methods of deconvolution and cross-correlation, both over directly and higher-order neighboring electrodes. The aim is to find out if there is merit to combining these two methods, particularly in relatively complex settings of cardiac electrical conduction. To this end, we introduce simulated sections of cardiac tissue with increasing degrees of different forms of conduction block and multiple sources of electrical stimulation. We will evaluate how the proposed combination compares not only to the baseline method of steepest deflection, but also to the use of each of the constituent parts on their own.

1.3. Thesis outline

This thesis is divided into six chapters, organized as follows. Chapter 2 provides information on the background of the project. The basic anatomy of the heart, along with the properties of its electrical conduction are introduced. Details of atrial fibrillation are given, along with an introduction of epicardial mapping and an overview of current methods for estimating LATs from the measurements produced by such a mapping procedure. In Chapter 3, the proposed method for processing the electrograms to estimate the LATs is introduced. A detailed description is given of its constituent parts, deconvolution and cross-correlation over higher-order neighbors. Chapter 4 describes and discusses the methodology used for generating simulated electrogram data, introducing the metric used to judge performance of different LAT estimation methods on the data. Using this simulated atrial data, Chapter 5 quantitatively compares the performance of the methods developed in Chapter 3 to reference methods as illustrated in Chapter 2. In Chapter 6, a summary and discussion of the obtained results are given, and resulting topics for possible future research are proposed.

2

Background

This chapter provides the background necessary to effectively understand the contents of the subsequent chapters of this thesis. We introduce key concepts related to the human heart at a fundamental level, as well as more low-level theories on its functioning and the associated electrical activity, which play a role in cardiac arrhythmias such as atrial fibrillation. In Section 2.1, information is given on the functioning of the heart, with an overview of basic cardiac anatomy, a model for electrical activity at the cellular level, and an introduction on surface electrocardiograms and how they relate to underlying cardiac activity. Section 2.2 goes into detail on the cardiovascular disease of atrial fibrillation, its manifestations, theories on its causes and current forms of treatment. Section 2.3 describes methods for measuring the electrical activity of the atria directly on the tissue and how the resulting measurements can be interpreted. Finally, Section 2.4 reviews different methods for obtaining and quantifying from these measurements the activation times of the cells in the measured tissue, which can subsequently be used to estimate the activation pattern of the cardiac cells.

2.1. Electrical activity of the human atria

2.1.1. Basic anatomy of the heart

As one of the most important organs in the human body, the heart plays a key role in supporting major processes vital for sustaining human life. The main function of the heart is to pump blood around the body. Nutrients and oxygen are supplied to the different parts of the body by this blood through a system of blood vessels, and waste products such as carbon dioxide are disposed of. Fig. 2.1 shows a schematic frontal section of the heart, with key components indicated. The main part of the heart are its four chambers. The two smaller, superior chambers are the left and right atria; the two larger, inferior chambers are the left and right ventricles. The outside layer of the heart is known as the epicardium; the inside layer of the heart is known as the endocardium, with myocardium lying in between. Four valves (the cream-colored components in Fig. 2.1) control the flow of blood between the chambers and the arteries connected to them. The bicuspid and tricuspid valves are situated between the atrium and ventricle on, respectively, the left and right side of the heart; the pulmonary and aortic valves are situated between the ventricles and the corresponding connecting arteries.

The left and right chambers are separated from each other, with each being part of respectively the large and small circulatory system, interconnected through the lungs. Blood from the upper and lower caval veins, low in oxygen and rich in carbon dioxide, enters the right atrium and gets pumped to the lungs via the pulmonary artery connected to the right ventricle. After exchange of gases in the lungs, the blood, now oxygenated and depleted of carbon dioxide, enters the left atrium via the pulmonary veins. Flowing to the left ventricle, it is then pumped into the aorta to reach the different parts of the body [22].

2.1.2. Electrical conduction in cardiac cells

The activity of the muscle cells in the heart (known as cardiac muscle cells or cardiomyocytes) is regulated by electrical signals. These signals propagate through muscular tissue and cause the cardiomyocytes to contract. Although it can appear that way when viewed at the scale of the full heart, the

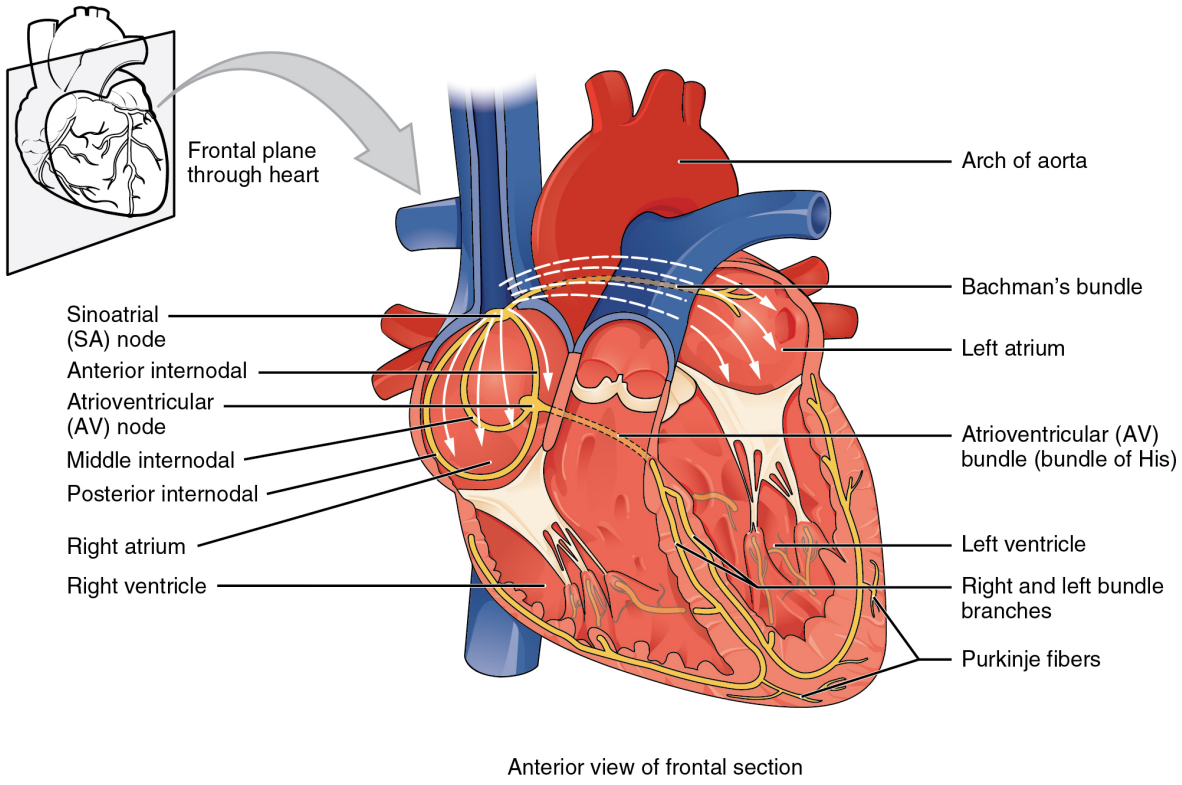

Fig. 2.1: Frontal cross-section of the heart, showing the basic anatomy of the atria and the ventricles, with the most important electrical conduction pathways indicated in yellow. Adapted from [23, p. 848].

propagation of the signals does not happen in a continuous manner. Rather, it goes step by step. When a cell is depolarized (activated), it in turn triggers its neighboring cells to depolarize, a process which causes the signal to be conducted throughout the tissue of cardiomyocytes. A network of pacemaker cells regulate this activity and determine the rate of contraction. The process of regular contraction of the heart muscle involves a number of such components that guide the conduction of electrical signals across the heart, indicated in Fig. 2.1 in yellow. The origin of the process is the sinoatrial (SA) node (located in the right atrium), where the cardiac electrical impulses normally stem from. The resulting rhythm of regular cardiac contraction controlled by the SA node is known as sinus rhythm (SR). This initial impulse propagates from the SA node across the atria, reaching the left atrium via a group of cardiomyocytes known as Bachmann's bundle. Thus, the atria contract first, after which the impulse is carried further to the atrioventricular (AV) node and on to the ventricles via the bundle of His. This conduction to the ventricles is relatively slow, to allow the ventricles to fill with blood before they contract and pump the blood into the arteries, completing the cardiac cycle [22].

The conduction of electrical signals across the muscle cells of the heart does not happen as easily in all directions: it is an anisotropic phenomenon (i.e., not isotropic), which fact is reflected in a differing conduction velocity (CV) depending on the direction. Signals in general are more readily conducted in the longitudinal than the transversal direction, due to the orientation of the myocytes relative to each other. This effect is illustrated in Fig. 2.9, which shows the conduction of a signal through an area of cardiac cells. The arrows indicate the mean direction of propagation, corresponding to the longitudinal direction (along the fibers) of the cardiac cells. The degree of anisotropy can be quantified by the anisotropic ratio, defined in cardiomyocytes as the ratio between the CV in the longitudinal and the transversal directions [24].

2.1.3. Action potentials and propagation in the atria

The activation of cardiomyocytes in the SA node amounts to depolarization of the local cells, which corresponds to a shift in the electrical potential of the cells. This is caused by excitation from neighboring cells or another source. The resulting pattern of the course of this cell potential over time as the cell

is activated is known as the action potential (AP). The type of cell determines the morphology of this AP, as Fig. 2.2 shows. This figure also shows the pattern followed by atrial muscle cells: multiple flows of ions across the cell membrane during the depolarization and repolarization process cause the visible changes in potential. Inward flows of sodium and calcium ions, as well as a number of different currents of potassium ions, are thought to be the chief actors controlling the AP [25]. Two important parameters that characterize the AP are the activation time and the refractory period. The activation time is defined as the moment when the potential of the cell reaches a certain threshold during the depolarization phase; this determines whether an AP is triggered in the cell, or not. The refractory period is the minimum period after activation of a cell during which no subsequent AP can activate the cell. This period is typically a bit shorter than the full duration of an AP, which helps prevent the heart from contracting in too rapid a manner [26].

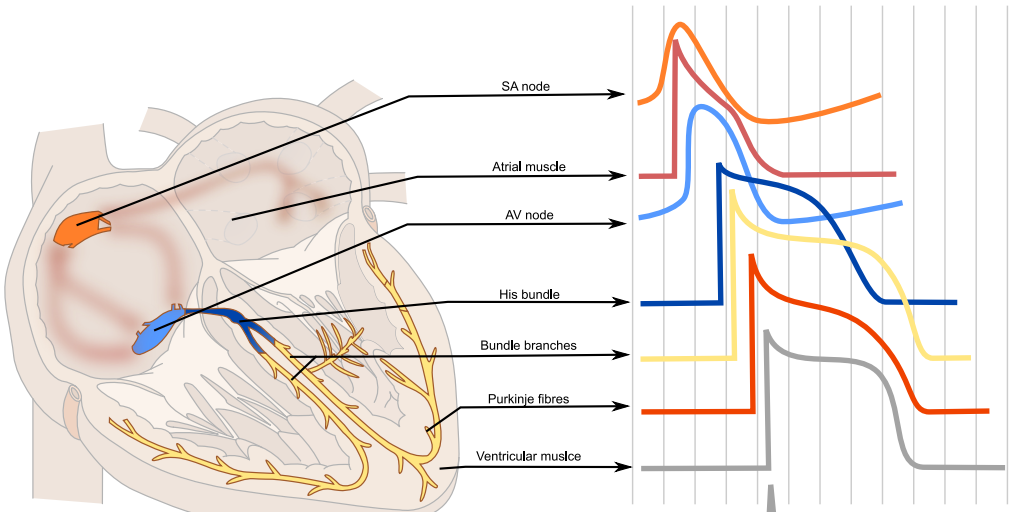

Fig. 2.2: Varying morphologies of the AP generated by cells in different locations in the heart. Adapted from [27].

To model the spatial propagation of an AP through cardiac tissue, a mono-domain approximation [28] is used; the cardiac tissue in this approximation is discretized on a two-dimensional grid. In the widely used model by Courtemanche *et al.* [29], the propagation of the AP from cell to cell in this mono-domain formulation is modeled as a reaction–diffusion system. This implicitly defines the transmembrane cell potential V_{m} at location $\mathbf{x}$ and time t as

$$C_{\mathrm{m}} \frac{\partial V_{\mathrm{m}}(\mathbf{x},t)}{\partial t} = I_{\mathrm{tm}}(\mathbf{x},t) + I_{\mathrm{stim}}(\mathbf{x},t) - I_{\mathrm{ion}}(\mathbf{x},t,V_{\mathrm{m}}), \tag{2.1}$$

where C_{m} is the membrane capacitance, and I_{tm}, I_{stim} and I_{ion} are respectively the transmembrane, stimulation and total ionic current. The total ionic current is a summed representation of the ionic activity in the cell membrane (e.g., inward and outward currents through ion pumps). The constituent currents of I_{ion} are themselves dependent on the potential V_{m} and specific ion conductivities [29]. The transmembrane current accounts for the diffusion (i.e., spatial evolution or propagation) of the transmembrane potential, according to

$$I_{\mathrm{tm}} = S_{\mathrm{v}}^{-1} \boldsymbol{\nabla} \cdot (\boldsymbol{\Sigma}(\mathbf{x}) \boldsymbol{\nabla} V_{\mathrm{m}}(\mathbf{x},t)). \tag{2.2}$$

Here, S_{v} is the cellular surface-to-volume ratio and $\boldsymbol{\Sigma}(\mathbf{x})$ is the position-dependent extracellular conductivity tensor. It contains information about the electrical conductivity of the tissue in different directions at location $\mathbf{x}$, incorporating directional differences related to the anisotropic ratio as well as information on areas of lower conductivity. Comparing (2.2) with (2.1), we can thus see that the spatial propagation and temporal evolution of V_{m} (represented by the divergence and gradient operators on the one hand and the first-order time derivative on the other hand, respectively) are interrelated. The transmembrane current will show up again later, when we use it to model the potential measured by an electrode in the vicinity of the cardiac tissue.

2.1.4. Electrocardiograms

The electrical activity of the heart, described in the previous sections, can be measured and quantified in various ways. Arguably the best-known modality for representing this activity is the surface electrocardiogram (ECG), which is measured by applying electrodes to the surface of the body (i.e., on the skin). The potential that this measures is effectively a spatial average of the activity of all heart cells. Willem Einthoven was the first to accurately measure this using a string galvanometer [14], measuring and recording a current using electrical leads connected to the extremities of the patient. Over the years, various improvements were made to the measuring technique, leading to the 12-lead electrocardiogram (ECG) method widely used today, which utilizes 10 electrodes placed on the limbs and the chest [15]. An example of a standard electrocardiogram can be seen in Fig. 2.3. It shows the change of potential over time, often printed on grid paper. The characteristic shape of the ECG when measured during SR, first described by Einthoven [13], consists of a P wave, a QRS complex, and a T wave. Each of these can directly be related to specific parts of the cardiac cycle, as Fig. 2.4 illustrates. The P wave is the main marker of atrial activity, corresponding to depolarization of the atria. The remaining part of the signal is related to ventricular activity: the QRS complex corresponds to the depolarization and the T wave to the repolarization of the ventricles. The repolarization of the atria is not visible in the ECG, as it is concealed by the larger-amplitude QRS complex.

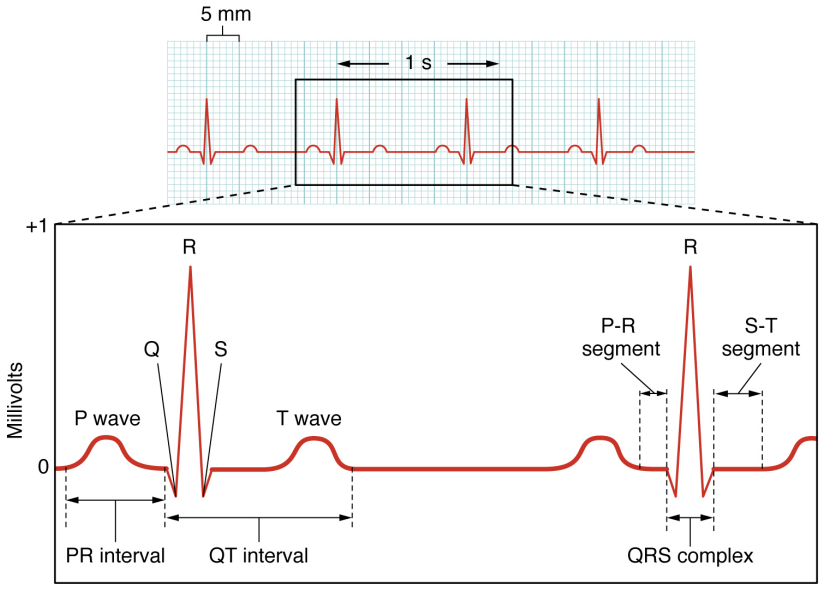

Fig. 2.3: Example of a surface electrocardiogram, annotated to indicate characteristic features present in sinus rhythm. Adapted from [23, p. 855].

2.2. Atrial fibrillation

There are various ways in which the regular beating of the heart, described in the previous section, can be disrupted and irregularities introduced. Diseases that affect the heart in this way are referred to as cardiac arrhythmias. One type of cardiac arrhythmia is atrial fibrillation (AF): in patients with this condition, the regular depolarization of the cells in the atria is disrupted, leading to irregular, chaotic contractions of the atrial heart muscle. This decreases the efficiency with which the heart is able to pump blood around the body. AF is one of the most common age-related cardiac arrhythmias. Quantitatively, this amounts to 1 to 3 percent of the European population suffering from AF, this proportion increasing in the elderly. It is becoming increasingly prevalent as life expectancy increases, with the number of cases expected to double by 2060 [10]. In itself, AF is mostly asymptomatic and not directly a grave condition. However, it can lead to a number of other, more serious conditions, such as blood clots, stroke, and heart failure [9], [10]. Moreover, AF can lead to ventricular fibrillation, where the ventricles beat rapidly and irregularly. This is an acute life-threatening condition, with sudden cardiac death following in absence of treatment [30].

AF can manifest itself in different ways, ranging from short, incidental episodes to continuous fibrilla-

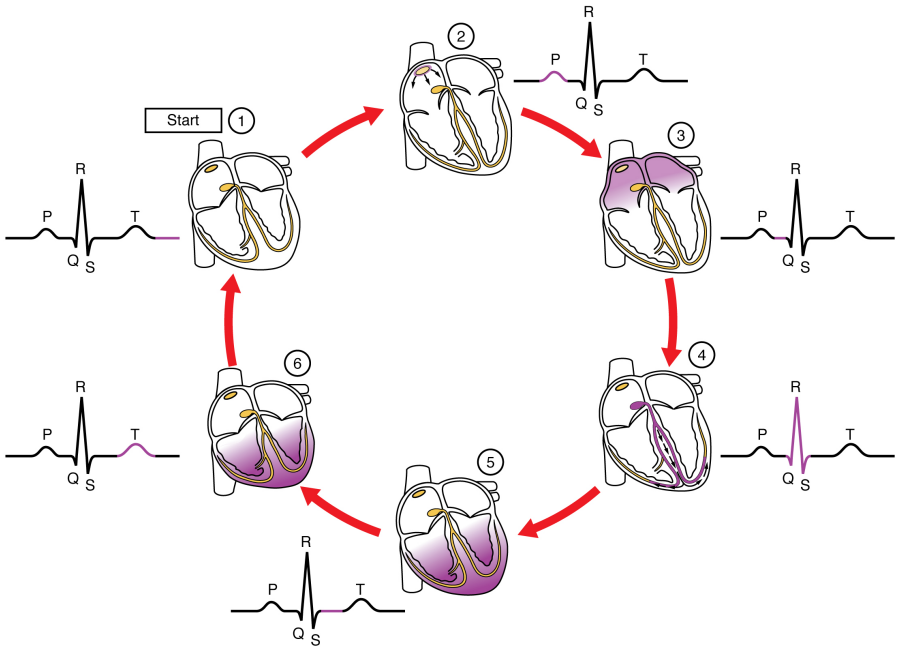

Fig. 2.4: Relationship between the different parts of the cardiac conduction cycle and the segments of a surface ECG. Adapted from [23, p. 856].

tion. This facilitates classifying it according to the length and frequency of occurrence. The corresponding types of AF in this system are paroxysmal (episodic, spontaneous bursts), persistent (continuous fibrillation) and permanent (chronic, continuous fibrillation, not responding to treatment) [31]. It has been found that paroxysmal AF can exhibit a progressive nature, with episodes becoming longer and more frequent [32], increasing the risk of other complications developing.

The most common way to diagnose AF is by using an ECG. In patients suffering from AF, a clear deviation in morphology from the one encountered in SR can be seen; this is illustrated by Fig. 2.5. The regularly spaced heartbeats in SR are replaced during AF with heartbeats showing irregular intervals between successive peaks of ventricular activity, as is indicated by the varying intervals between R peaks. Furthermore, the P waves present in SR are absent during AF (the larger waves that are visible beside the R peaks are T waves), caused by unsynchronized electrical activities in the atria. In their place, we see low-amplitude fibrillatory waves, known as f waves [33].

2.2.1. Mechanisms

In search of a model responsible for governing AF, numerous studies have been done into the generation and maintenance of the condition. Accordingly, various theories and mechanisms have been put forward. An early theory was formulated by Moe *et al.*, who proposed that the propagation of multiple wavelets through the atria causes AF to sustain itself [35], [36], producing an unorganized atrial rhythm. Up to the present day, in spite of the many hypotheses that have been published since, no clear consensus has been reached [12]. Debate on the subject is ongoing, making this a topic that is not completely understood.

Nevertheless, there are a number of mechanisms for AF that commonly appear in literature; these can be seen in Fig. 2.6. The far left of the figure illustrates the phenomenon of *ectopic foci*: this corresponds to spontaneous impulses originating from locations other than the SA node and interfering with sinus activity. This has been shown to be a possible cause of AF [37]. The concept of *rotors*, indicated in the middle left of the figure, is related to *reentry*, which corresponds to an activation wave effectively traveling in a circular path around a block in conduction, such as scar tissue, and re-exciting the cells. Rotors are a functional, dynamic manifestation of regions of reentry, which can be stationary or move through tissue, stimulating AF [37]. Recent studies have found that AF can also be initiated by asynchrony between the endocardial and epicardial sides of the atria [38]–[41]. In such a setting, an activation wave propagates unequally through different layers of muscle cells. This can lead to an ap-

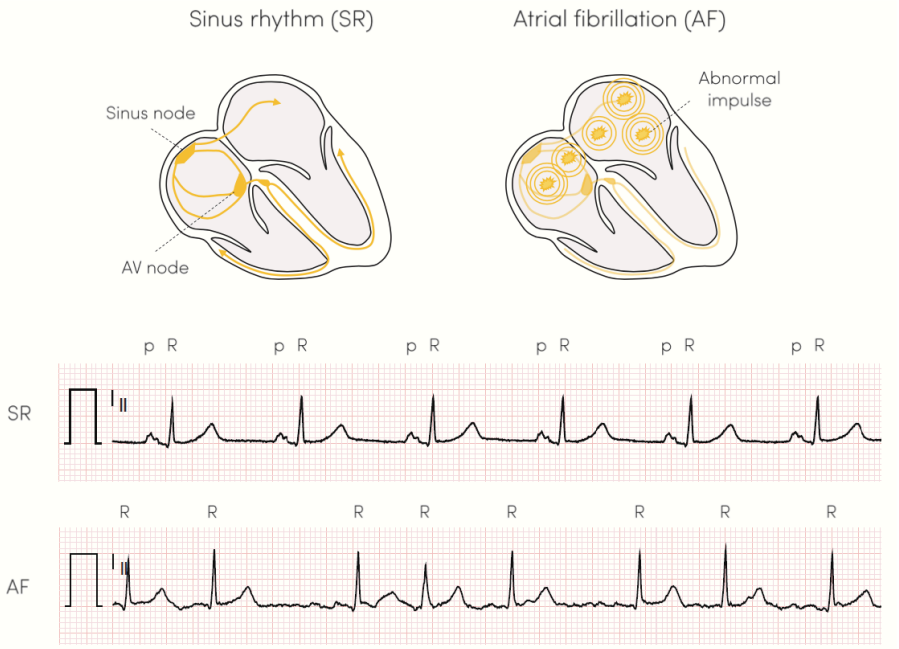

Fig. 2.5: Cardiac electrical conduction during normal sinus rhythm (SR) and during atrial fibrillation (AF). The upper panel shows how during SR (left), electrical activity is regularly initiated at the sinus node, after which it spreads to the AV node via the right atria and continues on to the ventricles. During AF (right), abnormal impulses cause chaotic activation of the atria, leading to distorted activation of the ventricles. The lower panel shows two ECGs, measured during SR and AF. During SR, P waves are present and the R peaks are spaced regularly. During AF, the P waves are absent and the intervals between R peaks are irregular. Adapted from [34, p. 12].

parent activation source appearing at the epicardial surface, a phenomenon known as *endo–epicardial breakthrough*. This is illustrated in the middle right of Fig. 2.6. The far right of the figure represents an example of the *wavelet* theory mentioned before. These wavelets are thought to originate from a propagating activation wave that gets broken into smaller components on encountering a conduction barrier. As a result, smaller wavelets propagate in different directions, with possibly different velocities, promoting the sustaining of AF and causing chaotic activation of atrial tissue [42].

These potential mechanisms of AF are not mutually exclusive: viewed in complement, they can give a better idea of the underlying causes of the condition. Furthermore, different interpretations of the same underlying physiological process could be extracted from the same tissue depending on the measurement and analysis methods employed [43, p. 14]. In any case, research suggests that an important contributor to the initiation and maintenance of AF is to be found in the realm of impaired conduction and damage on a structural level in atrial muscle tissue, such as fibrosis (scarring of the cardiac tissue) [44], [45]. This makes the challenge of obtaining a clearer, more comprehensive view of the degree of conduction impairment in tissue increasingly relevant for getting to the bottom of AF.

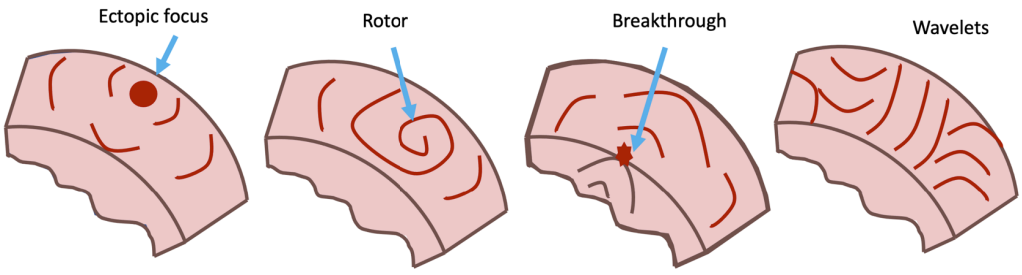

Fig. 2.6: Illustration of different mechanisms of atrial fibrillation on a section of cardiac tissue. Adapted from [43, p. 14].

2.2.2. Treatment

Different methods have been developed to treat certain forms of AF. With a progressive condition like AF, treatment has a higher chance of success if the defect is diagnosed early. We can distinguish between two forms of treatment: pharmacological methods (through the use of medication) and electrical methods. Drugs are often used as the first option in the treatment of spontaneous AF: they can be used to prevent blood clots, limit the heart rate to safe levels and restrict the frequency of ventricular activity. Medication also exists which maintains SR in patients with paroxysmal AF, available for regular consumption or at the onset of an AF episode [46].

A common form of electrical treatment is ablation therapy, which seeks to eliminate the origin of a disturbed signal or the tissue responsible for conducting it. It is a minimally invasive treatment: a catheter is typically inserted in the groin area and guided to the heart via blood vessels, reaching the heart via the inferior caval vein. This catheter thus gains access to the inside of the heart, where it is used to scar or otherwise destroy the relevant section of cardiac tissue (often either by applying a very high or very low temperature to the area). A typical form of this technique is pulmonary-vein isolation (PVI), which scars the atrial tissue connecting the pulmonary veins to the heart with the aim of isolating AF triggers originating there [12]. This method may not be effective in patients with longer-term forms of AF, such as persistent AF, where multiple triggers may be responsible for the symptoms encountered. Such patients can benefit from other forms of ablation, performed in concert with PVI, such as AV node ablation, which prevents disorganized atrial signals from propagating to the ventricles [47], and linear ablation, which creates lines of scar tissue [48]. It is also possible to seek out and find the AF triggers during surgery, guided by a catheter that measures the electrical signals at different locations in the tissue [49].

Overall, the success of different treatment strategies is still limited by a lack of understanding of the inner workings of AF. A success rate of up to about 75% can be reached using catheter ablation, but this requires multiple procedures [50]. Treatment could thus benefit dramatically from increased understanding of the causes and mechanisms behind AF and the perpetuation of the condition.

2.3. Epicardial mapping of electrical activity

The previous section illustrated the need for an accurate way to measure and represent the electrical activity of the atria. ECG recordings can be used to get a sense of the organization of cardiac contraction, as we explained in Sections 2.1.4 and 2.2. While a useful non-invasive way to diagnose AF, conventional ECGs are less suited to obtain a detailed view of atrial conduction (though specifically tailored surface-potential systems have been investigated for such a use, as in [51]). Due to the relatively large distance between the electrodes and the heart, the spatial resolution is coarse, resulting in a measurement that provides only a spatial average of the underlying activity. If we sacrifice non-invasiveness, much more information can be obtained. Recording atrial electrical activity by placing closely spaced electrodes directly on the heart, known as *epicardial mapping*, is a good method for achieving this end. It provides us with a spatio-temporal recording of electrical activity, allowing us to track wavefronts as they propagate through atrial tissue.

Obtaining information about the time and location of electrical activity through epicardial mapping consists of multiple steps. The first step in the mapping process consists of acquiring epicardial potential measurements, known as electrograms (EGMs), using an array of electrodes. In the second step, these EGMs are interpreted and processed to estimate the activation pattern of the underlying tissue. There are various techniques for measuring EGMs, with the spatial dimension being sampled in different ways. This includes measurements done in the form of electrodes attached to a needle at different heights to sample the depth direction in the heart [52]. Studies have also been done on the endocardial side, where, as in the ablation therapy mentioned in Section 2.2.2, a catheter is guided to the inside of the heart from the femoral vein. In the atria, the electrode array expands and takes the form of a “basket”, pressing against the curved endocardium [53].

To accurately map the epicardial surface, Yaksh *et al.* at the Erasmus University Medical Center used a high-resolution two-dimensional array, recording atrial activity during SR and induced AF [16]. A picture of the array can be seen in Fig. 2.7a. It consists of 192 electrodes of diameter 0.45 mm, positioned on a flexible 8-by-24 array with 2 mm separating each pair of electrodes. The whole of the left and right atria, as well as Bachmann’s bundle, was mapped using this array by placing it sequentially on 9 different anatomical locations, shown in Fig. 2.7b. AF was induced by electrical stimulation of the

right atrium at a rapid rate. The high-resolution mapping studies performed using this method form the basis for the research in this thesis.

More recently, a variant of the array depicted in Fig. 2.7a was developed, that allows for simultaneous measurement of the endocardial and epicardial surfaces [38], [39]. The measurement apparatus used here essentially consists of two arrays similar to the one in [16], connected to the inside of the ends of a tong. A small incision in the right atrial appendage was made, after which one end of the tong was inserted to map the endocardium.

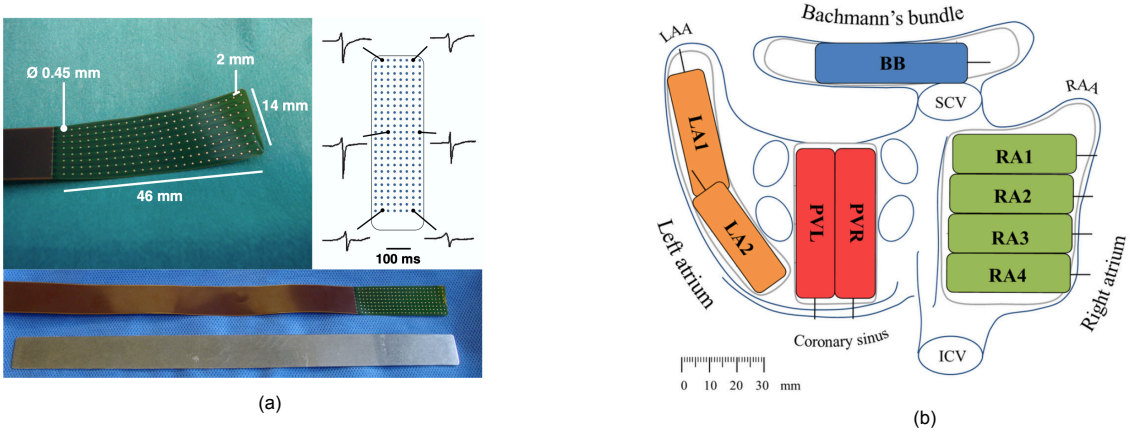

Fig. 2.7: Schematic overview of the epicardial mapping approach used at Erasmus University Medical Center. (a) Close-up of the mapping array containing 192 unipolar electrodes, along with examples of electrograms recorded at different points in the array, and the bendable steel spatula to which the array is attached. Adapted from [16]. (b) Projection of the electrode array on schematic posterior view of the atria, showing measurement locations. BB, Bachmann's bundle; ICV, inferior caval vein; LA, left atrium; LAA, left atrial appendage; PV, pulmonary veins; RAA, right atrial appendage; RA, right atrium; SCV, superior caval vein. Adapted from [54].

2.3.1. Electrograms

The electrical activity can be measured using electrodes applied to the surface of the heart, resulting in the electrograms mentioned in the previous section. Fig. 2.8A shows how the morphology of a measured electrogram relates to the vicinity of the wavefront propagating in the underlying tissue. As the action potential nears the electrode, the measured EGM (the potential at the electrode location) is increasingly positive, turning into a steep negative deflection as the tissue directly underneath the electrode is activated and the current passing underneath the electrode is maximal. As the AP moves away from the electrode, the EGM shows a gradual return to the baseline, starting value. In Section 2.1.2, a model for the transmembrane current was given, represented by (2.2). If we assume that the extracellular conductivity σ_e is homogeneous and isotropic, the EGM can be modeled using a current-source approximation for a large-volume conductor [28]. This gives

$$\phi(\mathbf{y}, t) = \frac{1}{4\pi\sigma_e} \int \frac{I_{tm}(\mathbf{x}, t)}{\|\mathbf{y} - \mathbf{x}\|} \, d\mathbf{x} \tag{2.3}$$

for the EGM at time t measured at electrode location $\mathbf{y}$. The integration variable $\mathbf{x}$ corresponds to the location of the cells. From (2.3), we can see that the measured signal is a sum of the activity of a large area of cells. Each of these cardiac cells contributes to the measured electrogram through its transmembrane current, weighted depending on the distance to the electrode, represented by $\|\mathbf{y} - \mathbf{x}\|$. Electrical activity of the ventricles, despite what the relatively large distance from measurement locations on the atria would suggest, can (and often does) show up as a significant (undesired) contribution of atrial electrograms, due to its relatively large amplitude [55].

The form of EGM described above is measured with respect to a fixed reference, located elsewhere on the body, and is known as a unipolar EGM. There are other variants, such as the bipolar EGM; this corresponds to the potential difference between a pair of electrodes. Fig. 2.8B shows the difference in standard morphology between unipolar and bipolar EGMs: where the point of local activation (marked as "LAT") corresponds to the steepest part of the deflection in a unipolar EGM, it corresponds to the minimal point of a bipolar EGM [56]. Bipolar EGMs, through their spatially differential nature, offer the

advantage that they can effectively filter out far-field ventricular interference, which reaches the different atrial electrodes at roughly the same time. The big disadvantage, though, is that due to their direction-dependency, they can filter out atrial activity as well, if the orientation of the electrodes is rotated with respect to the direction of AP propagation [57], [58]. In this thesis, as in the setup of [16], unipolar EGMs are considered.

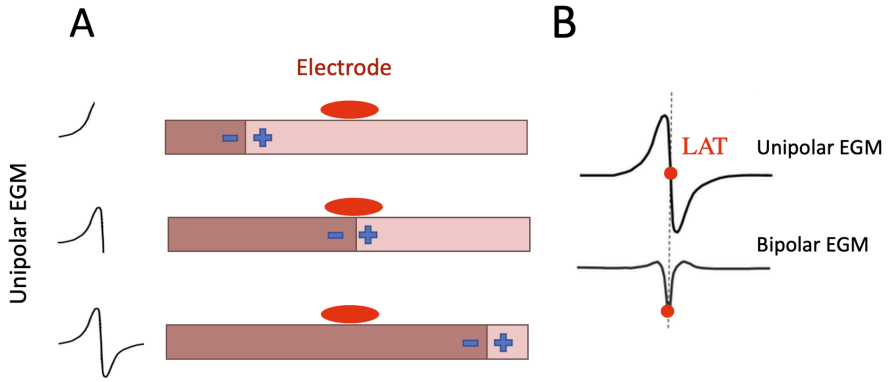

Fig. 2.8: Illustration of normal electrograms. (A) shows the generation of a unipolar electrogram in relation to the polarization wave in the tissue, and (B) shows an example of simultaneously recorded unipolar and bipolar electrograms. Adapted from [43, p. 12].

2.3.2. Interpreting cardiac data

Once the physical part of the epicardial mapping is complete and the electrical activity of the atria has been recorded, the measured electrograms can be interpreted. As mentioned in the previous section, unipolar atrial electrograms can suffer from far-field interference due to activity from the ventricles. Ideally, we would like to have recordings available that contain atrial activity only. During sinus rhythm, atrial and ventricular activity can be clearly distinguished, as atrial and ventricular contraction occur in an organized way. Ventricular activity is neatly preceded by atrial activity (an effect also visible in ECGs, as Fig. 2.5 shows). Time-domain windowing would suffice to extract the atrial activity here. During AF, however, activity of the upper and lower chambers can overlap temporally, making distinguishing between the two more difficult. A trade-off must then be made between preserving the atrial component of the signal and suppressing the ventricular component. Various methods have been developed to eliminate far-field ventricular activity in atrial electrograms to deal with such scenarios [55], [59], [60]. The electrograms we consider in this thesis are assumed to have ventricular activity removed.

With atrial activity isolated, an initial inspection of the epicardial EGMs can already provide valuable information. As Fig. 2.9 shows, the relative complexity of measured electrograms can give an indication of the state of organization of the underlying cardiac tissue. In healthy tissue with homogeneous conduction, electrical activations can spread through the tissue in a regular, albeit anisotropic way. This homogeneous conduction produces a relatively simple morphology in the electrogram, with one clear deflection. In diseased tissue, electrical conduction can be blocked or impaired in certain directions—this is known as *remodeled* tissue. This results in inhomogeneous conduction, giving rise to electrograms with multiple significant deflections.

A commonly used way of representing the activation of a section of cardiac tissue and making these effects visual is through the use of an activation map (AM). This gives a compact way of conveying the most important information of the depolarization wave contained in the measured EGMs. An example of an AM can be seen in Fig. 2.10: each square corresponds to an electrode of the measurement array pictured in Fig. 2.7a. The color corresponds to the time at which the local section of tissue is activated. This time point is derived from the measured EGM at that electrode, as illustrated by Fig. 2.8. An AM can therefore show where delays in conduction arise, as well as the path (and number) of activation waves in the tissue. Fig. 2.10 shows how, in sinus rhythm, the activation wave (singular) propagates through the tissue smoothly. During AF, the propagation is much more chaotic, due to blocks in conduction (indicated by the thick black lines) and multiple apparent sources of depolarization (indicated by the arrows), which result in more than one activation wave moving through the tissue.

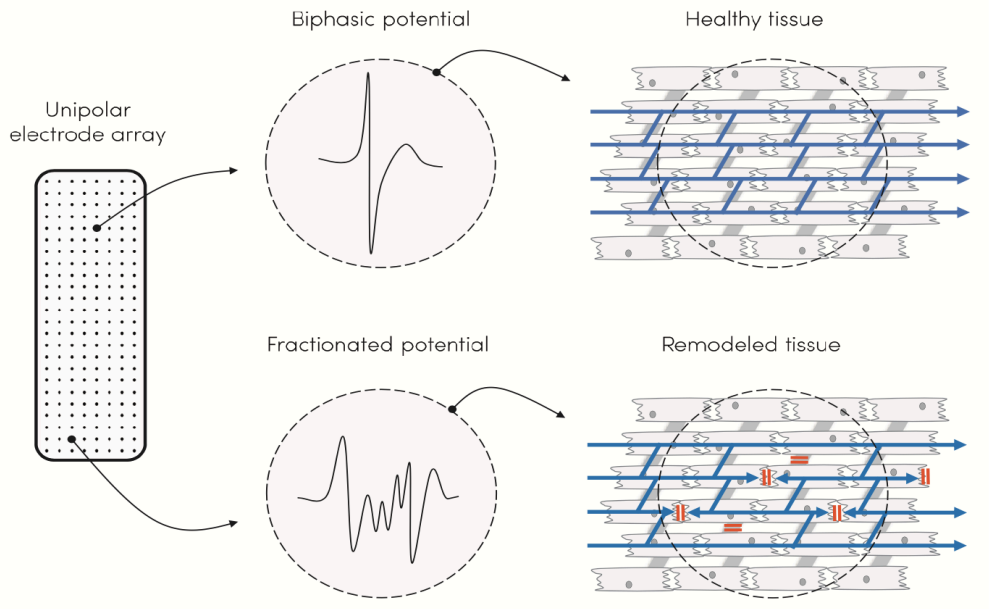

Fig. 2.9: Connection between the morphology of unipolar electrograms and organization of electrical conduction in the underlying cardiac tissue. Different electrodes on the mapping array on the left can measure electrograms with different morphologies, shown in the middle, with *biphasic* denoting a single deflection and *fractionated* denoting the existence of multiple significant deflections. The biphasic signal originates from healthy underlying tissue with homogeneous conduction, whereas the fractionated signal originates from *remodeled* tissue with inhomogeneous conduction. Adapted from [34, p. 19].

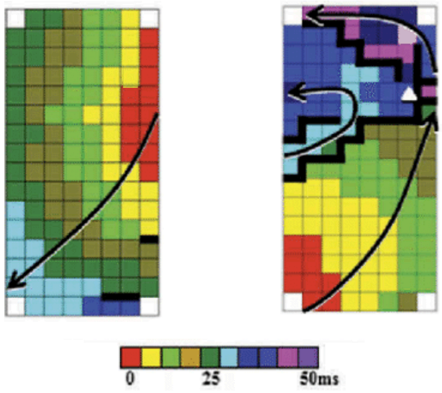

Fig. 2.10: Two activation maps, recorded during sinus rhythm (left) and atrial fibrillation (right). The direction of depolarization waves is indicated by black arrows and conduction blocks are shown as thick lines. Adapted from [61].

2.4. Local activation times and methods for annotation

An essential part of estimating the activation pattern in epicardial mapping, as detailed in the previous section, is determining the time point at which the tissue underneath each sensor (electrode) in the array is activated. This comes down to estimating the local activation time (LAT) for that particular sensor location. Fig. 2.8 gives a visual example of how the LAT relates to the depolarization wave propagating through the tissue. In the previous section, we also saw how activation maps, a visual representation of the LATs, are a useful tool to exemplify the variations in electrical conduction in different cardiac settings, as illustrated by Fig. 2.10. If the LATs are available, they can be used to calculate the conduction velocity, which can in turn be used to quantify mechanisms involved in sustaining AF, like reentry, multiple wavelets, and conduction blocks (indicated by a low conduction velocity). Hence, an accurate estimation of LATs is important for improving treatment methods of AF.

A model for the atrial electrogram ϕ was given by (2.3). We saw that the measured potential is influenced by the activation of multiple cells (captured by the transmembrane currents), weighted by the distance of those cells to the electrode. As the action potential propagates across different cells, the

corresponding transmembrane currents of those cells are not synchronized. Thus, as cells with different moments of activation contribute to the electrogram, the result is that for each electrode i at location $\mathbf{x}_i$, for $i = 1, 2, ..., M$, with M the total number of electrodes, the corresponding electrogram ϕ_i registers a combination of all the activation times of the cells in the area. The objective in the estimation of LATs can be described as extracting the true LAT τ_i of electrode location $\mathbf{x}_i$ from the measured electrogram ϕ_i. Because of the averaging of cell activity inherent in the electrogram, this can pose quite a challenge.

In the most basic form of estimation, no automation is used at all, and the LAT is annotated manually in each electrogram by a physician. This has obvious drawbacks: it is time and labor intensive, and the accuracy of this method can be difficult to determine, owing to its subjective nature. Different experts may interpret the same electrogram in different ways. Recording electrograms in an array gives us spatio-temporal information which we can use to aid and automate the LAT estimation process. Different (automated) methods have been developed to obtain these LATs exploiting various aspects of the measured data [17]. In this section, the most widely used of these algorithms are presented.

2.4.1. Steepest deflection

In the most commonly used method for LAT estimation, the time derivative of the electrogram is used. In unipolar electrograms, the point at which this quantity reaches its minimum (i.e., the point at which the negative deflection is steepest) was shown to correspond well to the time of activation in the underlying tissue [56], [62]. This time point, known as the steepest deflection (SD), has been shown to have a physiological connection to cellular processes in the tissue: it is related to the moment when the transmembrane sodium current is maximally increasing [63]. For electrode i, given the corresponding electrogram $\phi(\mathbf{x}_i, t)$, the LAT is obtained using this scheme as

$$\tau_i = \arg\min_t \frac{\mathrm{d}\phi(\mathbf{x}_i, t)}{\mathrm{d}t}. \tag{2.4}$$

While this method has the advantage of being relatively easy to implement and quite intuitive, it has notable disadvantages. It does not take into account spatial information, as each electrogram is evaluated individually. The effect of surrounding electrodes is therefore disregarded. Using the time derivative of the measured signal poses a risk in itself: it makes the method sensitive to small spikes in the signal, caused by noise sources in the measurement. Furthermore, although the time derivative has a strong connection to the action potential on a microscopic scale, this connection becomes weaker when viewed in a macroscopic context, such as in epicardial mapping. As more cells now play a role in the electrogram, with more distant cells possibly adding larger contributions to the derivative, the derivative can become less related to true local cellular activity [18].

2.4.2. Spatial gradient

Instead of looking at temporal changes, as is the case with SD, the spatial evolution of epicardial electrical activity can also be investigated. An example is the method where the spatial gradient is used to estimate the LATs [64]. This utilizes the high spatial current density as an action potential propagates through tissue. Viewing the potential in two dimensions, the surface spatial gradient of the electrogram is defined as

$$\boldsymbol{\nabla}\Phi = \frac{\mathrm{d}\Phi}{\mathrm{d}\mathbf{x}} = \left[\frac{\mathrm{d}\Phi}{\mathrm{d}x}, \frac{\mathrm{d}\Phi}{\mathrm{d}y}\right]^{\mathsf{T}}, \tag{2.5}$$

where Φ is a spatial representation of all electrograms ϕ_i arranged according to their locations $\mathbf{x}_i$. The gradient is calculated for each electrode using the four neighboring electrodes, according to a central difference method. The LAT is then estimated by finding the time point where this spatial gradient achieves its maximal magnitude for each electrode,

$$\tau_i = \arg\max_t \|\boldsymbol{\nabla}\phi(\mathbf{x}_i, t)\| \tag{2.6}$$

for electrode i, where $\boldsymbol{\nabla}\phi(\mathbf{x}_i, t)$ is the spatial gradient at time t at electrode location $\mathbf{x}_i$.

The surface Laplacian can also be used as a modality of spatial information; this is defined using the divergence of (2.5) as $\nabla^2\Phi = \nabla \cdot \boldsymbol{\nabla}\Phi$. The Laplacian locates the wavefront of activation as the points which separate the current sources preceding the wavefront from the current sources following the wavefront. The LAT then follows as the time of the zero crossing of the Laplacian [64], [65].

2.4.3. Time-domain cross-correlation

A different way to incorporate information embedded in the spatial dimension of the electrode-array recordings is to consider the relative time delay between the signals measured by different electrodes [20]. For signals that have a similar morphology (and that can therefore be said to be correlated), this can be accomplished by using the cross-correlation operation. For electrodes i and j, with $i, j = 1, 2, ..., M$, measuring electrograms ϕ_i and ϕ_j over K time samples, the cross-correlation $\rho_{(i,j)}$ at lag s can be expressed as

$$\rho_{(i,j)}(s) = \frac{1}{K\sqrt{\sigma_i^2 \sigma_j^2}} \sum_k \left(\phi_i(k) - \mu_i\right)\left(\phi_j(k-s) - \mu_j\right). \tag{2.7}$$

Here, $k = 1, 2, ..., K$; μ_i and μ_j are the means of ϕ_i and ϕ_j, respectively; and σ_i^2 and σ_j^2 are the variances of ϕ_i and ϕ_j, respectively, used for normalization of the correlation value (such that $\rho \in [-1, 1]$). Using (2.7), the delays are considered for pairs of neighboring electrodes [20]. Let $N(i)$ denote the set of neighbors of electrode i. Then, the delay between electrode i and j is estimated as

$$\hat{\Delta}_{(i,j)} = \arg\max_s \rho_{(i,j)}(s), \tag{2.8}$$

for all $j \in N(i)$. With estimated delays between neighboring electrode pairs now available, they need to be converted to the LATs for each of the electrodes [17], [20]. Shors *et al.* expanded on this method by using the Hilbert transform of the cross-correlation [66] for a finer time resolution [67]. Kölling *et al.* developed it further, cross-correlating not only over direct, but also higher-order neighbors [21]; this will be further elaborated upon in Chapter 3.

The main limitation of this method lies in the fact that it requires signals that are similar up to a time shift. If the signals that are cross-correlated have less comparable morphologies (as can be the case in electrograms measured during AF), the cross-correlation will provide a less reliable and less meaningful estimate of the delay.

2.4.4. Deconvolution

A more fundamental approach to finding the LATs relates to the mathematical operation of convolution. For the functions f, g, and h of the continuous variable t, the convolution operation between f and h corresponds to the integral of the product between the two, after reversing and shifting one of the functions, defined as

$$g(t) = (f * h)(t) = \int_{-\infty}^{\infty} f(\tau) h(t - \tau)\, \mathrm{d}\tau. \tag{2.9}$$

This type of relation has some similarities to the cross-correlation operation used earlier. A convolution is often used to model the way a system h responds to a certain input f, resulting in the output g, defining a forward relation between f and g. If we want to obtain f from g, this is called an inverse problem. Deconvolution is a way to solve such a problem, an effort to "undo" the convolution. Generally, some prior knowledge is needed to be able to solve this, such as an estimate of one of the functions, denoted by $\hat{h}(t)$. An estimate of the desired function f can then be obtained by minimizing a cost function

$$\hat{f}(t) = \arg\min_f \left\| g(t) - (f * \hat{h})(t) \right\|, \tag{2.10}$$

which expresses the error between the estimate and the known data captured in g. Obtaining sufficiently accurate prior knowledge to get a useful estimate for f is often a challenge, which can be exacerbated by disturbances that can distort known data in g.

In an electrophysiological context, this operation comes into play when we look at the relation between an electrogram and the underlying transmembrane currents. The currents can be seen as an input, convolved with the "system" of cardiac tissue, resulting in an output corresponding to the electrogram measured on the epicardium. The epicardial electrogram was modeled in terms of the transmembrane currents by (2.3), which can be seen as a convolution, where the system response primarily corresponds to a weighting inversely proportional to distance. This leads to an electrogram that is effectively a blurred representation of the true cardiac activity represented by the currents. The microscopic scale of these phenomena makes it infeasible to directly measure the currents (although research has

been done on finding current estimates in dogs using a very fine, sub-millimeter-diameter electrode grid [68]), which makes deconvolution a more logical approach. Deconvolution techniques can be used in this setting to get an estimate for the input signal f (related to the LATs) or the system h (corresponding to the tissue conductivity pattern).

Different methods have been developed to deal with this problem, each employing their own form of *a priori* knowledge to make it feasible. Ellis *et al.* used an assumption of an activation wave traveling through tissue with a constant CV to get an estimate of the system response and the activation time [69]. *A priori* knowledge of the system response in the form of a known distance kernel was used in [70] along with a wavelet-filtering approach to estimate the transmembrane currents and LATs (the term "wavelet" here refers not to the wavelet theory of AF described in Section 2.2.1, but to the signal-processing concept of the wavelet transform [71]). Based on a simplified model of atrial conduction, Abdi *et al.* proposed a formulation of the inverse problem, using it to estimate tissue conductivity [72] and LATs [19]. The latter application is explained in more detail in Chapter 3.

2.4.5. Template matching

Activation of cardiac tissue can also be mapped using electrogram templates. In such a setup, segments or specific complexes of measured electrograms are compared to a reference library of electrogram deflection templates. Various methods exist to build and populate this library, using either mathematically derived complexes [73], [74], or parts of clinically recorded electrograms [75]. This can be of use in analyzing the complex activation patterns that can be encountered during AF, with electrograms showing complexes of multiple deflections. The similarity of the measured signals with the library templates is judged using a correlation function, resulting in a correlation coefficient and an estimate of the LATs, in a method similar to what was described in Section 2.4.3. Making the templates adaptive by minimizing an error function has been suggested to improve robustness in LAT estimation [75].

3

Processing atrial electrical data

In this chapter, the proposed methodology for estimating the LATs, which combines two existing algorithms, is presented. The electrical conduction across the epicardium can be (and often is) compromised in patients with AF, leading to measured electrograms of a complexity that can cause the performance of existing algorithms to suffer. To counter this, we perform preprocessing on the electrograms by deconvolution. This effectively performs a more local estimation of the underlying cardiac activity, through which equivalent, "clearer" transmembrane currents are obtained. Exploiting further the spatial structure of the data, these currents are then cross-correlated over higher-order neighbors to obtain pairwise delays between electrodes, after which the LATs are obtained through a least-squares minimization.

In Section 3.1, we describe a model of the measured electrograms, and based on this we propose a two-part system for extracting the LATs. In Sections 3.2 and 3.3, these two parts of the algorithm are explained in more detail.

3.1. Overview

3.1.1. General signal model

In Section 2.1.3 and 2.3.1, a model of the electrical activity in the atria was given, along with the parameters involved in producing the electrogram that is measured on the epicardial surface. We saw there that action potentials propagate in myocardial cells, causing a wave of contraction spreading through the atria (and later through the rest of the heart). The associated flows of different types of charged particles can be viewed as one transmembrane current per cell, dependent on tissue conductivity.

If we assume that the part of tissue of interest has homogeneous conductivity and negligible curvature, an electrogram as measured could then be modeled as a scaled and shifted version of a "standard" electrogram response $\phi_0(k)$ from the tissue. This corresponds to the response of the tissue to an activation wave traveling through tissue of uniform conductivity below an electrode [76]. Let M denote the total number of electrodes. This then gives an approximate model for a measured electrogram as

$$\phi_i(k) \approx \alpha_i \phi_0(k - \tau_i) + n_i(k), \tag{3.1}$$

for $i = 1, 2, \ldots, M$, with k the time index. Here, the scalar α_i determines the amplitude, τ_i denotes the time delay with which the signal is measured, and $n_i(k)$ is the measurement noise for electrode i. In this simple scenario, the different electrodes measure the same stereotype (reference) signal ϕ_0, up to a scaling and time-shift difference. Thus, electrode j will measure effectively the same electrogram $\phi_i(k)$ of electrode i, but with a different amplitude and with a delay. Using cross-correlation (as in Section 2.4.3), we could then well obtain an estimate of the delay between two electrodes, as they are scaled and shifted versions of each other [76].

If we take a step forward from this simple scenario and introduce anisotropy and heterogeneous conduction profiles, the approximation of (3.1) can become less accurate. In such a context, the heterogeneous conduction in the tissue can amount to conduction blocks, with electrical propagation differing depending on direction. This can result in multiple activations being detected, spread out in time [76],

leading to an approximate signal

$$\phi_i(k) \approx \alpha_i \phi_0(k - \tau_i) + \sum_j \beta_j \phi_0(k - \tau_j) + n_i(k), \tag{3.2}$$

where the model of (3.1) has been extended with a second term, modelling the additional activations as disturbances, scaled by β_j at time delays τ_j [76]. When only one of these waveforms actually corresponds to the true local epicardial activation, it can become difficult to distinguish this from the other disturbances, more distant counterparts. Furthermore, disturbances in one signal may be present at different delays than compared to another signal. Obtaining inter-electrode delays by cross-correlation thus becomes more difficult and less reliable, as the true activation in one electrode could, for example, be erroneously correlated with a disturbance in another.

3.1.2. System outline

In tackling the problem of estimating the LATs from measured electrograms as in (3.2), we have seen that relying on cross-correlation alone can be prone to errors. We therefore propose combining a cross-correlation method with a second step: an extra processing step is inserted in between measuring the EGMs and obtaining the LATs. Fig. 3.1 gives a schematic overview of this system. This extra step consists of deconvolving the input EGMs (introduced in Section 2.4.4), in order to get a clearer, more local view of the electrical activity of the atria.

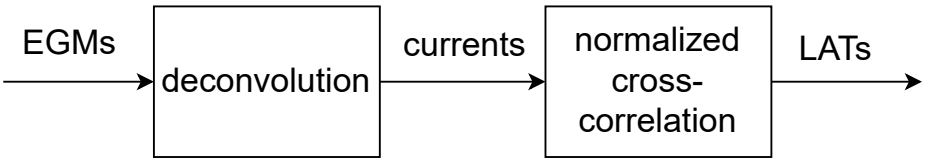

Fig. 3.1: Schematic overview of the proposed system.

The transmembrane-current estimates that this produces will, in effect, make the model of (3.2) better to work with for the cross-correlation step, which is now applied not to the electrograms themselves but to the time derivative of the transmembrane current, as the next section will explain. This second step is provided with a less opaque view of the electrical activity in the tissue of interest: the deconvolution operation practically attenuates the distant disturbances and emphasizes local activity captured in the EGMs, corresponding in (3.2) to relatively smaller β_j terms compared with α_i. Therefore, across different electrodes, the local activity at those points is more likely to be the main peak in the cross-correlation sequence between them, improving the accuracy of the LAT estimation.

3.2. Deconvolution

The first part of the proposed algorithm is based on work by Abdi *et al.* [19], [77], [43, Ch. 5], and expands on the model described in Chapter 2 and seeks to extract a less "blurred" view of the cardiac electrical activity from the electrograms in the measurement area. In accordance with (2.3), electrograms can be viewed as a weighted spatial sum of the underlying transmembrane currents in the neighborhood of the electrodes. For the electrogram Φ at time t_c and sensor location (x_m, y_m), where $m = 1, 2, \ldots, M$, this relationship can be described [78, p. 236] as

$$\Phi(x_m, y_m, t_c) = \frac{1}{4\pi\sigma_\mathrm{e}} \int_{\mathcal{A}} \frac{I(x_c, y_c, t_c)}{\sqrt{(x_c - x_m)^2 + (y_c - y_m)^2 + z_0^2}} \, \mathrm{d}A(x_c, y_c). \tag{3.3}$$

Here, σ_e denotes the constant extra-cellular conductivity, $\mathcal{A}$ denotes the modeled cells over which the sum is taken, z_0 is the (constant) electrode height and $A(x_c, y_c)$ is the area variable.

Equation (3.3) can be seen as a spatial (i.e., two-dimensional) convolution of the transmembrane current I with a weighting function. To make this explicit, let R_0 be a distance-kernel operator, defined as

$$R_0(x_c, y_c) = \frac{1}{\sqrt{x_c^2 + y_c^2 + z_0^2}}. \tag{3.4}$$

This effects the weighting of cell activity inversely depending on the distance to an electrode. Furthermore, let S_0 be a sampling operator, defined as

$$S_0(x_c, y_c) = \sum_{m=1}^{M} \delta(x_c - x_m)\delta(y_c - y_m), \tag{3.5}$$

such that only the cells corresponding to electrode locations are sampled. This models the spatial sampling effected by the electrode array. Combining the expressions for R_0 and S_0 with the model of (3.3), we can formulate the model explicitly as a convolution, as

$$\Phi(x_c, y_c, t_c) = \frac{1}{4\pi\sigma_{\mathrm{e}}} S_0(x_c, y_c) \left(R_0(x_c, y_c) * * I(x_c, y_c, t_c)\right), \tag{3.6}$$

where the symbol $**$ is used to indicate the two-dimensional convolution operation.

The deconvolution algorithm thus seeks to recover the transmembrane currents I from the measured electrogram potentials Φ. This is done by minimizing the mean-square error between the measured electrograms and reconstructed versions of the electrograms as

$$\min_I \left\|\Phi - S_0(R_0 * * I)\right\|_2^2 + \lambda \left\|I'\right\|_1, \tag{3.7}$$

where the l_1-norm is a regularization term and the spatial and temporal arguments have been left out for ease of notation. The l_1- and l_2-norms present in (3.7) are defined as

$$\|I\|_2^2 = \sum_x \sum_y \sum_t |I[x, y, t]|^2, \quad \left\|I'\right\|_1 = \sum_x \sum_y \sum_t |I'[x, y, t]|. \tag{3.8}$$

Intuitively, one could see how the optimization of (3.7) could be difficult: the number of available electrograms ("known" data points) is smaller than the number of modeled cells, meaning that information is lost through the convolution operation. Moreover, the distance kernel R_0 effectively has a low-pass filtering effect. Indeed, such inverse problems in general, as in this case, are highly ill posed, resulting in unstable solutions [19].

To alleviate this issue, some form of *a priori* knowledge on the target quantity I is required. The key assumption we make in this regard is that the electrogram contains one or more sharp deflections, which can be seen in the time derivative I' of the current. A way to incorporate this condition is to ensure that I' is sparse, i.e., it only has a few non-zero elements, a reasonable assumption for most types of electrograms [19]. This condition is implemented in the problem of (3.7) by the regularization term consisting of an l_1-norm constraint, known to promote a sparse solution [79, p. 304].

To implement (3.7), the quantities involved are discretized across the sample grid and the sampled distance kernel by a limited support. This allows for translation into a matrix model; details on the discretized implementation of this algorithm can be found in [77].

An example of the effect of deconvolution on fractionated electrograms can be seen in Fig. 3.2. Four tissues with different conduction profiles [19, Fig. 2] were used to simulate cardiac electric propagation. From the activation maps in the first row (where white pixels correspond to cells that are positioned on a block and were therefore not activated), we can see that conduction delays and blocks in the cells surrounding the electrode produce fractionation in the electrograms Φ in the second row: each exhibit multiple deflections. The third row, portraying the time derivative of the electrograms Φ', shows that far-field disturbances are incorrectly labelled as the local activation. The fourth row, then, shows the desired effects of the deconvolution operation: in the time derivative of the current I', the far-field disturbances are attenuated and the local activity is amplified, leading to correct annotation of the local activation.

In [19], the output current is directly used to estimate the activation time, defining it as the time point where the steepest deflection, i.e., the minimum of the time derivative, occurs. Specifically, instead of I, the time derivative I' is thus used for LAT estimation (as Fig. 3.2 shows). Therefore, Abdi *et al.* solve the problem of (3.7) primarily with the aim of improved spatial accuracy of I'; this quantity is also the one in which the *a priori* knowledge is incorporated, as explained earlier. A result of this is that less importance is attached to the morphology of the currents I. Consequently, the morphology of the estimated I can vary quite significantly in practice across different spatial locations. This makes it less suited than I' for correlation-based processing, which is the next step of the proposed algorithm (as

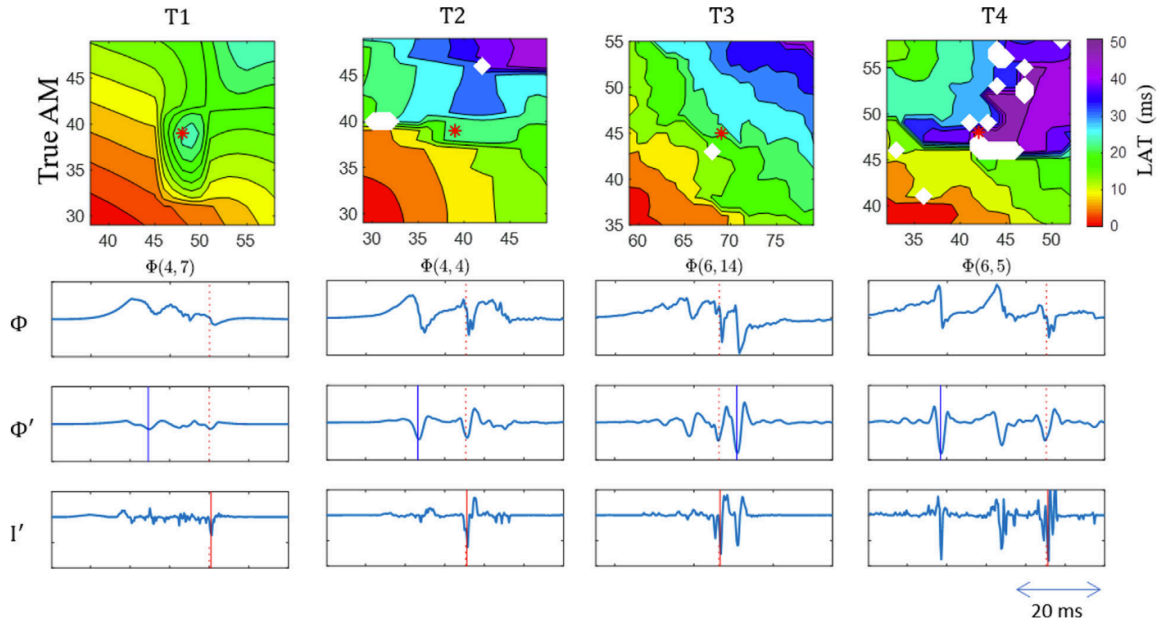

Fig. 3.2: Examples of different modalities of cardiac activity. T1 to T4 represent simulated sections of stimulated epicardium with varying conductivity profiles. The first row shows the ground-truth activation maps corresponding to each of the four profiles, with the red asterisk denoting the electrode location. The second row shows the electrograms recorded at those locations, with the dotted line indicating the true LAT. The third and fourth row show the time derivatives of the electrogram and the estimated current, respectively. The solid blue and red vertical lines indicate the steepest descent of the electrogram and the current, respectively. Adapted from [19].

was illustrated by Fig. 3.1 and Section 3.1.2). Hence, we use the time derivative of the transmembrane currents, I', as the basis for further processing. Instead of directly using it to find the activation times as in [19], we carry it on to the next processing step, which will perform the actual LAT estimation.

3.3. Cross-correlation over higher-order neighbors

This part of the algorithm, based on work by Kölling *et al.* [21], [76], adapts a methodology proposed in [20] to find the LATs by exploiting the spatial structure of the electrode array with which the electrograms are measured. First, relying on the one-stereotype-waveform assumption of (3.1), the delays between the signals of all electrode pairs are computed by considering their cross-correlation, exploiting the structure to determine which pairs are considered. Next, these obtained delays are converted to absolute LATs through least-squares processing.

3.3.1. Spatial structure and higher-order neighbors

The structure of spatial connections between electrodes can effectively be represented as a graph. We define a graph G as the tuple $G = (V, E)$, where V denotes the set of vertices and $E \subseteq V \times V$ denotes the set of edges. V in this setting corresponds to the electrodes in the array, spaced as a square grid. A simple way to represent the edges is by connecting each node to its direct neighbor. This, then, gives a graph as in Fig. 3.3(a). As each node is connected to a node one hop away, we can say that all first-order neighbors are connected. We can increase the number of edges by also connecting nodes more than one hop removed from each other. Let $G^{(P)}$ denote the grid graph where all nodes are connected to at most their Pth order neighbors. Fig. 3.3 shows three examples of such graphs $G^{(P)}$, featuring first-, second-, and third-order neighbors. The electrode array is defined as a square, 11-by-11 grid, so $|V| = M = 121$. From a quick look at the graphs, one can see how the complexity increases rapidly with the neighbor order as extra edges are added. From left to right, the graphs have an edge-set size $|E|$ of respectively 220, 618, and 1154 connections.

Returning to the $P = 1$ case, we can express the connectivity of the system by defining a $|V|$-by-$|V|$ binary adjacency matrix $\mathbf{A}$, whose entries are one if the corresponding nodes i and j are connected, i.e., $(i, j) \in E$, and zero otherwise. For $P > 1$, we can similarly look at the adjacency matrix of the

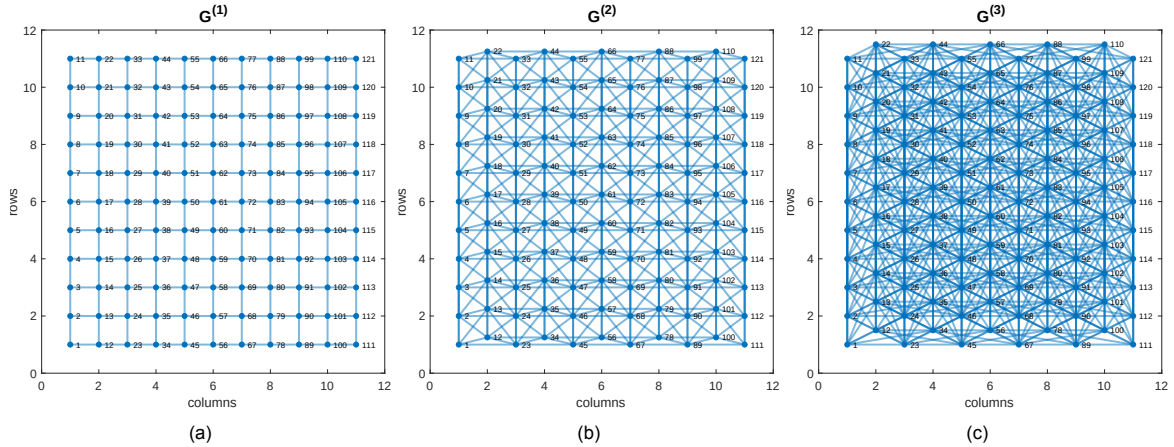

Fig. 3.3: Graphical representation of an 11-by-11 electrode array as a connected graph $G^{(P)}$, for $P \in \{1, 2, 3\}$.

resulting graph $G^{(P)}$. Defining it as $\boldsymbol{\Xi}^{(P)}$, we can express it in terms of the first-order adjacency matrix as

$$\boldsymbol{\Xi}^{(P)} = \sum_{p=1}^{P} \mathbf{A}^p - \operatorname{diag}\left(\operatorname{diag}\left(\sum_{p=1}^{P} \mathbf{A}^p\right)\right). \tag{3.9}$$

Here, the second term on the right-hand side ensures that $\boldsymbol{\Xi}^{(P)}$ is a valid, acyclic adjacency matrix by setting all diagonal elements to zero. The off-diagonal elements can now have values larger than one, but it still holds that non-zero elements correspond to connected nodes (up to P hops apart) and zero-valued elements correspond to unconnected nodes.

3.3.2. Obtaining LATs from pairwise delays

To determine the time delays in LATs of electrode pairs, the time-domain cross-correlation is used. We define the cross-correlation between electrograms ϕ_i and ϕ_j (both consisting of K time samples) at lag s in normalized form as

$$\rho_{(i,j)}(s) = \frac{1}{K} \sum_{k} \frac{\left(\phi_i(k) - \mu_i\right)\left(\phi_j(k-s) - \mu_j\right)}{\sqrt{\sigma_i^2 \sigma_j^2}} \tag{3.10}$$

for all electrode pairs (i, j) such that $[\boldsymbol{\Xi}^{(P)}]_{i,j} \neq 0$, i.e., for all pairs that are at most P hops apart. Here, μ_i and σ_i^2 are respectively the sample mean and sample variance of ϕ_i. The estimated delay $\hat{\Delta}_{(i,j)}$ then follows as the lag s that maximizes the cross-correlation $\rho_{(i,j)}(s)$.

Each estimated delay will differ from the true delay $\Delta_{(i,j)}$ by an estimation error $e_{(i,j)}$. Gathering all estimated delays in a vector $\mathbf{d}$ and relating them to the true delays, we can thus write

$$\mathbf{d} = \begin{bmatrix} \tau_2 - \tau_1 \\ \tau_3 - \tau_1 \\ \vdots \\ \tau_j - \tau_i \end{bmatrix} + \begin{bmatrix} e_{(1,2)} \\ e_{(1,3)} \\ \vdots \\ e_{(i,j)} \end{bmatrix} \in \mathbb{R}^{|E|}, \tag{3.11}$$

where τ_i is the true activation time of electrode i. As each delay corresponds to the difference of the true LATs of connected nodes of $G^{(P)}$, each delay essentially corresponds to a weighted edge of $G^{(P)}$, captured in $\boldsymbol{\Xi}^{(P)}$. Therefore, the $|E|$ estimated delays $\mathbf{d}$ can be expressed as an offset linear combination of the M true LATs $\boldsymbol{\tau}$ through the graph's M-by-$|E|$ incidence matrix $\mathbf{B}$ as

$$\mathbf{d} = \mathbf{B}^{\mathsf{T}} \boldsymbol{\tau} + \mathbf{e}, \tag{3.12}$$

where $\mathbf{e} \in \mathbb{R}^{|E|}$ contains the estimation errors. Assuming the error terms are zero-mean and mutually uncorrelated, i.e., $\mathbb{E}[\mathbf{e}] = \mathbf{0}$ and $\operatorname{Cov}(\mathbf{e}) = c\mathbf{I}$ for positive real c, we can estimate the LATs using the ordinary least-squares estimator as

$$\hat{\boldsymbol{\tau}} = \left(\mathbf{B}\mathbf{B}^{\mathsf{T}}\right)^{-1} \mathbf{B}\mathbf{d}. \tag{3.13}$$

In a connected graph such as $G^{(P)}$, the rank of the incidence matrix is one less the number of vertices [80, p. 166], so $\mathrm{rank}(\mathbf{B}) = M-1$ in this case. Therefore, because $\mathbf{B}$ is rank deficient, (3.12) represents an under-determined system and the direct inverse in (3.13) cannot be used. To still solve (3.12), a pseudo-inverse can be used to find the LATs as

$$\hat{\boldsymbol{\tau}} = \left(\mathbf{B}^{\mathsf{T}}\right)^{\dagger} \mathbf{d}, \tag{3.14}$$

where $(\cdot)^{\dagger}$ indicates the Moore–Penrose inverse, which can be computed using the singular-value decomposition (SVD) of $\mathbf{B}^{\mathsf{T}}$ [81].

As mentioned before, this method of adding higher-order neighbors in the consideration of cross-correlations to find the inter-electrode delays [21] can be seen as an expanded form of a method where only the direct (i.e., first-order) neighbors are used for cross-correlation [20]. Comparing the two approaches, we effectively use $\boldsymbol{\Xi}^{(P)}$ with either $P = 1$ [20] or $P > 1$ [21]. In effect, these (relatively) distant delays provide extra information for the estimation of the LATs, which can be seen in the smaller sparsity of $\boldsymbol{\Xi}^{(P)}$ compared to $\boldsymbol{\Xi}^{(1)}$ and the larger size of $\mathbf{B}$ for $P > 1$ compared to $P = 1$. For example, for a central node, like node 61 in Fig. 3.3, increasing P from 1 to 2 already increases the number of delays used to estimate the LAT (corresponding to the degree of the node) from 4 to 12, as can be seen in Fig. 3.3(a) and Fig. 3.3(b).

4

Simulated atrial data

In this thesis we use simulated data of the electrical activity in the atria as an approximation of real, clinical settings. This allows us to get a sense of the performance of the system proposed in Chapter 3. In this chapter we explain how this data is generated.

In Section 4.1 we go into more detail on the model underlying the simulated data and the associated parameters that are used to model different types of cardiac activity. Section 4.2 then shows examples of what the resulting data can look like, relating the obtained simulated electrograms to the simulation setting, and, in Section 4.3, we illustrate the performance measure that we will use to judge the performance of LAT estimation methods on the simulated data.

4.1. Description of simulation data

In this section, we explain how we construct the sets of simulation data. Section 4.1.1 presents the forward model used to generate electrograms and Section 4.1.2 explains the different ways that sections of atrial tissue are generated to model various conductivity and stimulation settings. Finally, Section 4.1.3 details the way that measurement noise is taken into account in the simulations.

4.1.1. Simulation setup

To generate simulated electrograms, we follow the method of simulating electrical activity described in [72]. The basis for this model lies in the model of the action potential in the atria according to a monodomain reaction–diffusion equation [28], as described in Section 2.1.3. This allows electrograms to be generated based on transmembrane currents as a forward model [78, p. 236], leading to a compact model [72] for computation of the simulated electrograms as

$$\phi_m[t] = \frac{1}{4\pi\sigma_{\mathrm{e}}} \sum_{n=1}^{N_{\mathrm{c}}} \frac{I_{\mathrm{tm}}[\mathbf{x}_n, t]}{r_{m,n}} \Delta x^2, \quad m = 1, 2, \ldots, M, \quad t = 1, 2, \ldots, N_t, \tag{4.1}$$

which can be seen as a space–time-discretized version of (3.3). Here, the transmembrane current at time t and cell location $\mathbf{x}_n$ is indicated by I_{tm}. N_{c} denotes the total number of modeled cells, M denotes the total number of electrodes, and N_t denotes the total number of time points. The myocardial cells are assumed to lie on a two-dimensional rectangular square grid, spaced by Δx. The electrode array with which the electrograms are simulated to be measured is then assumed to lie in a plane parallel to the cells, at a height of z_0. This constant height gives an expression for the cell–electrode distance

$$r_{m,n} = \sqrt{z_0^2 + \|\mathbf{x}_n^2 - \mathbf{y}_m^2\|_2}, \tag{4.2}$$

where $\mathbf{y}_m$ corresponds to the (two-dimensional) location of electrode m in the plane of the electrode array [76].

4.1.2. Conductivity and stimulation profiles

With the model from the previous section, a number of different data sets were generated. The electrode array was implemented as a square, 11-by-11 grid, with a constant inter-electrode distance of 2 mm.

Underneath this array, a square area of cells is located, with an inter-cell distance Δx of 2/3 $\approx$ 0.7 mm (thus forming a 31-by-31 grid), on which the electrode array is centered. The distance of the electrode plane to the cell plane was set to 0.1 mm. To be able to generate accurate signals, the cell area was extended to beyond the boundaries of the electrode array, making for a total area of 89 by 89 cells. The simulations were run for 300 ms with a step size of 50 µs, or equivalently, a sampling frequency of 20 kHz. The obtained data was then downsampled to a frequency of 1 kHz, to match the sample rate used in a clinical setting [16] and thus to make the generated data more realistic.

To simulate different types of myocardium, three different cell conductivity patterns were generated, to model different ways the conduction between different areas can become decoupled (which can be caused by fibrosis in the heart [82]). The resulting patterns can be seen in Fig. 4.1. It should be noted that the cell area visible here corresponds to the 31-by-31 subset of the total area corresponding to the cells underneath the electrode array. For all patterns, the conductivity is viewed in a simplified, binary manner, where each cell can either have a value of 0 (a conduction block) or 1 (normal conduction). The first conductivity type, visible as S1 in Fig. 4.1, approximates percolation, a phenomenon where the tissue effectively becomes "a series of loosely coupled islands" in terms of its conductivity [83]. This is modeled by randomly disconnecting some modeled cells and their neighbors, thus appearing in an isotropic way as spots of conduction block in S1. The second conductivity pattern, S2, models zones of no conduction as a number of randomly positioned lines of blocks, providing anisotropic decoupling between cells on the grid [84]. The third pattern, S3, is a combination of the patterns in S1 and S2. As the locations of conduction block in all patterns are randomly generated, multiple realizations can be considered to check the consistency of the algorithm.

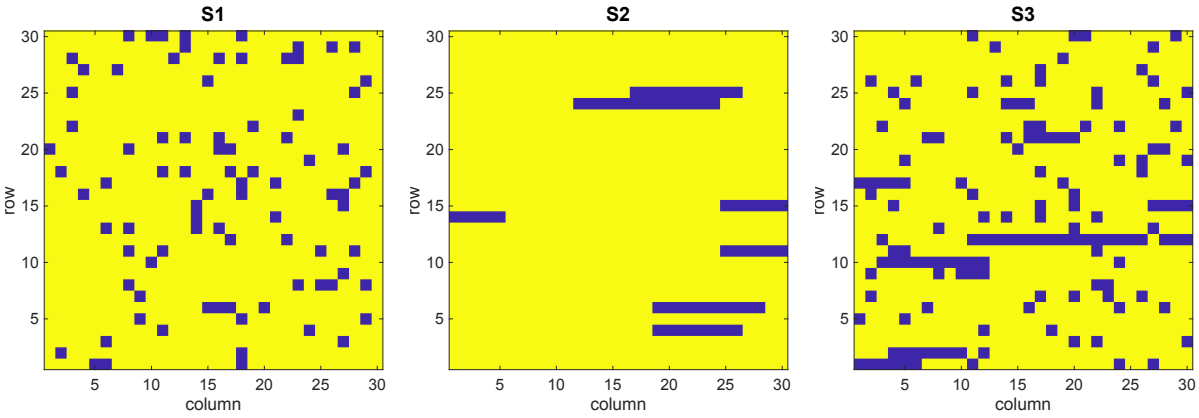

Fig. 4.1: Examples of randomly generated conductivity maps, each corresponding to a different kind of simulated fibrosis tissue. The conductivity values are normalized, with yellow areas corresponding to 1 and blue areas corresponding to 0.

In the simulated model, the propagation of action potentials through the cell area is started by stimulating a given cell with a current. This then leads to the depolarization of the first cells, after which the rest follows. To model different ways that cardiac activation wavefronts can originate and to create the ability to inspect the effect of multiple wavefronts on the electrograms, we defined two stimulation settings. For each of the conductivity patterns S1, S2, and S3 depicted in Fig. 4.1, we can thus investigate two further variations of setup. The two stimulation settings are depicted in Fig. 4.2. The figure shows the S1 conductivity setting over the complete, 89-by-89 cell area, along with the location of initial cell stimulation. The single-wavefront setting in Fig. 4.2a activates first the cell located in the bottom left of the cell area, outside of the measurement area. The other, triple-wavefront setting of Fig. 4.2b increases the number of wavefront sources from one to three and places each of them on the edge of the measurement area. All of the sources are activated at the same time.

4.1.3. Measurement noise

The model generating the simulated electrograms in (4.1) is based on physiological understanding of the atria. It does not, however, take into account external effects on the measured electrograms, i.e., effects on the measured signal caused by the actual performing of the measurement. To make the simulated data more similar to clinical data and thus more realistic, it is therefore good to incorporate

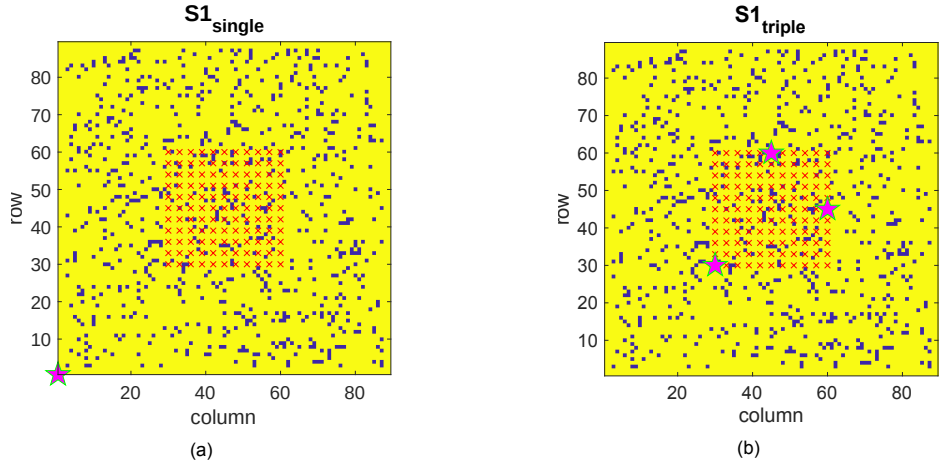

Fig. 4.2: The two different simulated stimulation settings. Overlaid on the yellow-and-blue conductivity map are the electrode locations in red and the location of the stimulated cells, indicated by magenta pentagrams.

measurement noise into our data. We do this by extending the model of recorded electrograms to

$$\mathbf{Y} = \mathbf{\Phi} + \mathbf{N} \in \mathbb{R}^{M \times N_t}, \tag{4.3}$$

where $\mathbf{Y} = \begin{bmatrix} \mathbf{y}_1 & \mathbf{y}_2 & \cdots & \mathbf{y}_M \end{bmatrix}^\mathsf{T}$, $\mathbf{\Phi} = \begin{bmatrix} \boldsymbol{\phi}_1 & \boldsymbol{\phi}_2 & \cdots & \boldsymbol{\phi}_M \end{bmatrix}^\mathsf{T}$, and $\mathbf{N} = \begin{bmatrix} \mathbf{n}_1 & \mathbf{n}_2 & \cdots & \mathbf{n}_M \end{bmatrix}^\mathsf{T}$ are the per-electrode components of respectively the measured signal, the electrogram potential (as modeled in (4.1)) and the noise stacked over all M electrodes. We model the measurement noise as additive Gaussian noise, uncorrelated spatially. Thus, for each electrode m we have an N_t-element noise term $\mathbf{n}_m \sim \mathcal{N}(\mathbf{0}, \sigma^2_{\mathrm{n},m}\mathbf{I})$. To unambiguously compare different noise levels, we use the signal-to-noise ratio (SNR), which we define in terms of the clean-signal and noise powers per electrode as

$$\mathrm{SNR} = \frac{P_{\phi,m}}{P_{\mathrm{n},m}} = \frac{\|\boldsymbol{\phi}_m\|_2^2}{\|\mathbf{n}_m\|_2^2} = \frac{1/N_t \, \|\boldsymbol{\phi}_m\|_2^2}{\sigma^2_{\mathrm{n},m}}, \quad m = 1, 2, \ldots, M. \tag{4.4}$$

Here, $\boldsymbol{\phi}_m$ contains the time-domain electrogram samples of one electrode. As each electrode will have a different electrogram power P_ϕ, the noise variance will similarly vary across electrodes to ensure an equal SNR.

4.2. Example of simulated electrograms

This example corresponds to the simulation setting $\mathrm{S3}_{\mathrm{triple}}$, i.e., cardiac tissue with lines and spots of block, electrically stimulated on three boundaries of the measurement area (see Fig. 4.1 and Fig. 4.2b). Fig. 4.3 shows the 11-by-11 ground-truth activation map, giving a graphical representation of the true activation time per electrode in this setting (the LATs are shifted in time in such a way that the first activation is at 0 ms). As was put forth in Section 4.1.1, the simulation generates transmembrane currents per cell, which then form the basis for the electrograms that are measured. Fig. 4.4 shows the true activation times of the same area as in Fig. 4.3, but now on a finer scale, per cell. The white area in the image corresponds to cells which did not activate and thus do not have an activation time. In this clearer view of the activity, the three source locations and locations of conduction block are more visible.

Four electrode locations have been highlighted: the electrograms corresponding to these points can be seen in Fig. 4.5. These signals, corresponding to the fifth row and columns eight to eleven of the electrode grid, exhibit multiple deflections, caused by the lines of conduction block in the tissue, and can thus be related to how the activation wave moves through the area. Fig. 4.6 shows the effect of measurement noise, as detailed in Section 4.1.3, on the obtained signals. Specifically, the electrogram of column 10 and row 5 is shown, first as a clean signal in Fig. 4.6a ($\mathrm{SNR} \to \infty$) and then in decreasing SNR levels to the right. At higher noise levels, more deflections appear in the signal that are not part of the underlying electrogram.

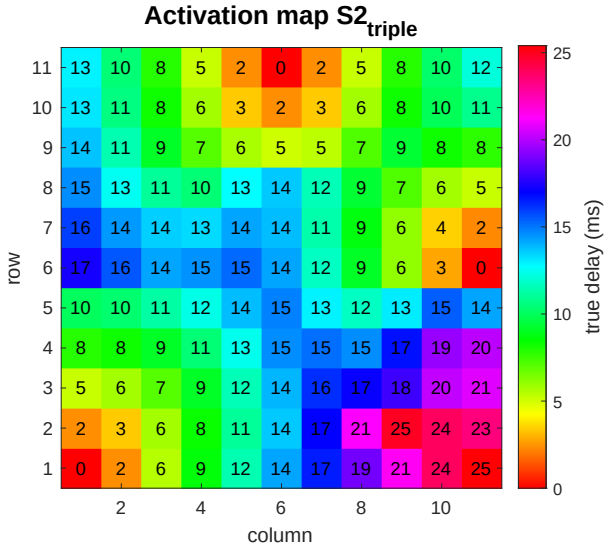

Fig. 4.3: Activation map for the electrode array, corresponding to the ground-truth activation times of conductivity pattern S2 and triple stimulation.

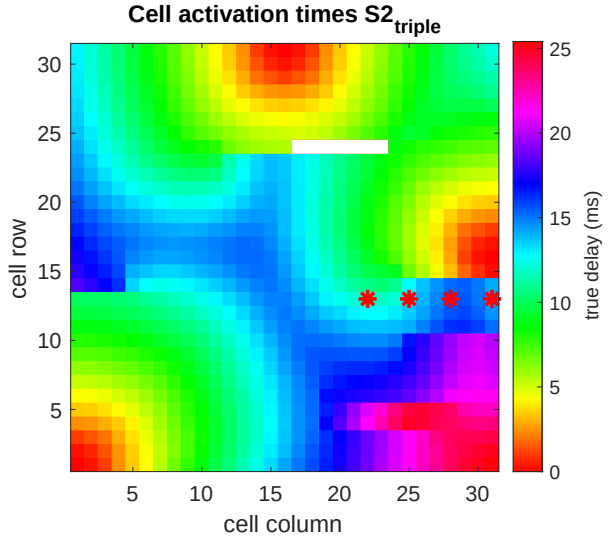

Fig. 4.4: Higher-resolution activation map, showing the true activation time for all cells with conductivity pattern S2 and triple stimulation. The red asterisks denote electrogram locations.

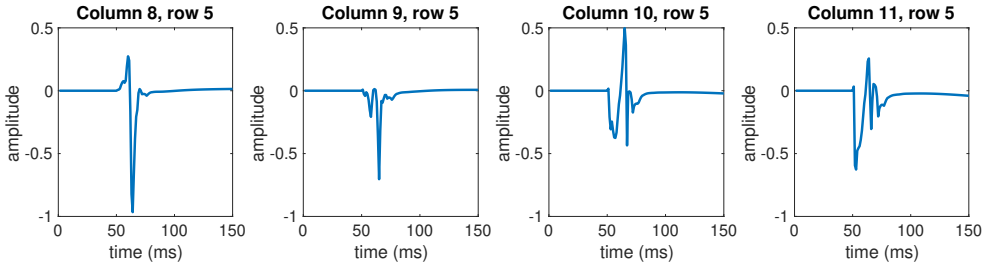

Fig. 4.5: Electrograms corresponding to, respectively, the four electrodes highlighted in Fig. 4.4 from left to right.

4.3. Quantifying accuracy of estimated LATs

4.3.1. Determining fractionation of electrograms

When considering the response of a section of atrial tissue to electrical stimulation, it is worth keeping in mind that some electrodes could be positioned above an area of relatively poor conduction, while

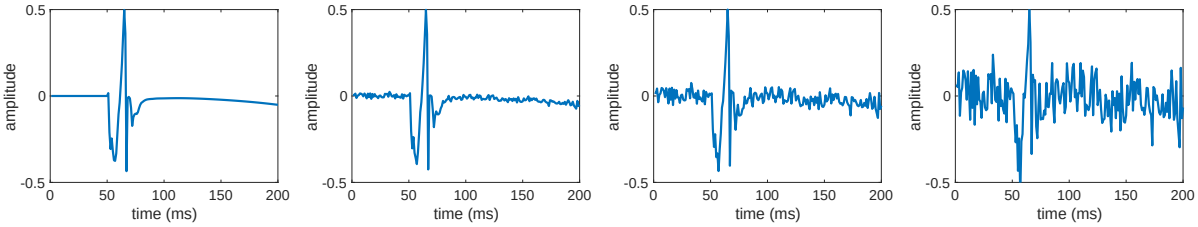

Fig. 4.6: The electrogram of column 10 in Fig. 4.5 for different noise levels. (a) The clean signal, and the signal with an SNR of (b) 20 dB, (c) 10 dB, and (d) 0 dB.

others might be present in normally conducting areas. We have seen in previous sections that the conductivity of tissue plays a large role in the resulting activity that can be measured. It can therefore be insightful to look at the performance of LAT estimation algorithms specifically at those electrodes where electrical conduction is poor and, as a result, the morphology of the recorded signal could be different from that of regular electrograms. In concurrence with literature, we will use the term *fractionated* to refer to electrograms exhibiting such irregular morphology. We have seen in Chapter 2 that the standard electrogram (recorded on epicardial tissue with normal electrical conduction) consists of one clear negative deflection. Consequently, if an electrogram shows two or more discernible negative deflections, we will classify it as fractionated [76].

4.3.2. Performance metric

To quantitatively weigh up different methods of estimating the LATs, we would like to have an objective metric to rank their performance. As we are working with simulated data, we have the advantage of having access to the ground-truth, i.e., true, LATs. We can use this to define the root-mean-square error (RMSE) for each LAT estimation method using a given data set as

$$\mathrm{RMSE} = \sqrt{\frac{1}{M}\sum_{i=1}^{M}(\tau_i - \hat{\tau}_i)^2}, \tag{4.5}$$

where M corresponds to the amount of usable electrodes (i.e., those corresponding to a ground-truth activation). Note here that this is not necessarily equal to the total number of electrodes. It can happen that the ground-truth activation time is not available: this could be the case if the corresponding electrode is positioned directly over a conduction block, in which case the corresponding part of tissue is not activated. To prevent such spurious outliers from dominating the RMSE and giving a misleading view of the performance, the LAT estimate for these points are eliminated from (4.5) and M is adjusted accordingly.

5

Results

With the method proposed in Chapter 3 and the simulation data described in Chapter 4, we can now evaluate the performance of the devised algorithm. This chapter describes the tests done and details the quantitative results this produced for the task at hand, which is estimating the LATs. In Section 5.1, the specific details of the used simulation data, in addition to what was described in Chapter 4, are described. The next two sections then give the main results: the proposed method of combining deconvolution and cross-correlation is compared with other existing strategies, using steepest deflection as a baseline. Specifically, we look at the use of increasing neighbor orders. Section 5.2 assesses the performance in simulated tissue with one point of electrical stimulation; Section 5.3 does the same for tissue with three sources of stimulation. A model for including measurement noise in the simulations was described in Section 4.1.3; the effects of different noise levels on the estimation results are investigated in Section 5.4.

5.1. Used data sets

The foundations of the data model used to generate simulation data was given in Section 4.1.1. We can effectively use this to test the different LAT estimation methods, as this setup also supplies us with the ground-truth activation times. Different tissue types, corresponding to different conductivity patterns (S1, S2, and S3), were described in Section 4.1.2, the precise layout of which is randomly generated. To avoid focusing too much on one specific realization, we generated ten random realizations of S1, S2, and S3. These simulated areas underneath the electrode array can be seen in Fig. 5.1, Fig. 5.2, and Fig. 5.3, respectively. With ten realizations of each pattern and an 11-by-11 electrode array, our simulation thus produces 1210 electrograms for each of the three patterns.

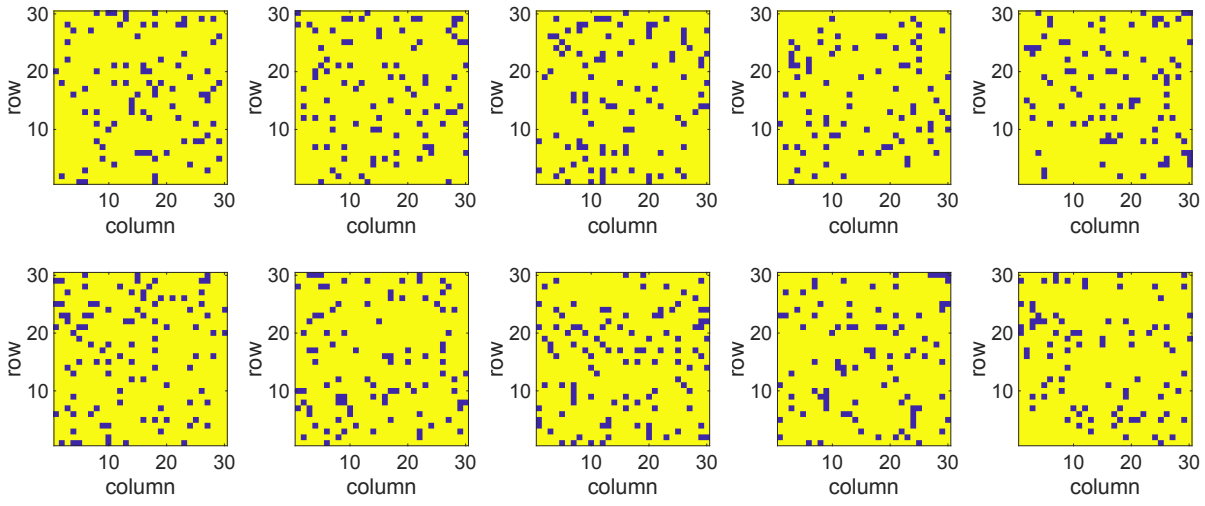

Fig. 5.1: The ten used realizations of the 31-by-31 normalized conductivity pattern for the cells in data set S1.

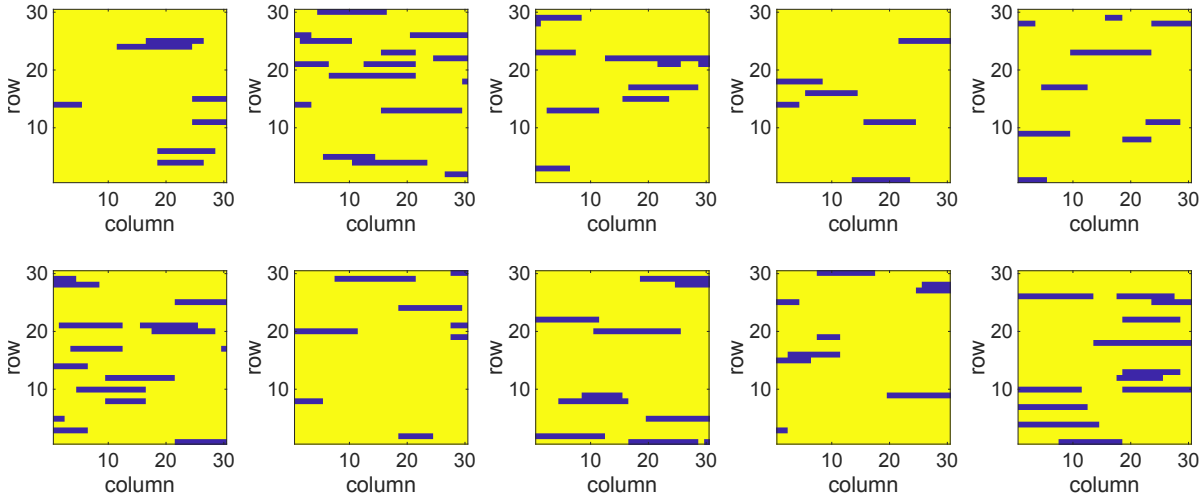

Fig. 5.2: The ten used realizations of the 31-by-31 normalized conductivity pattern for the cells in data set S2.

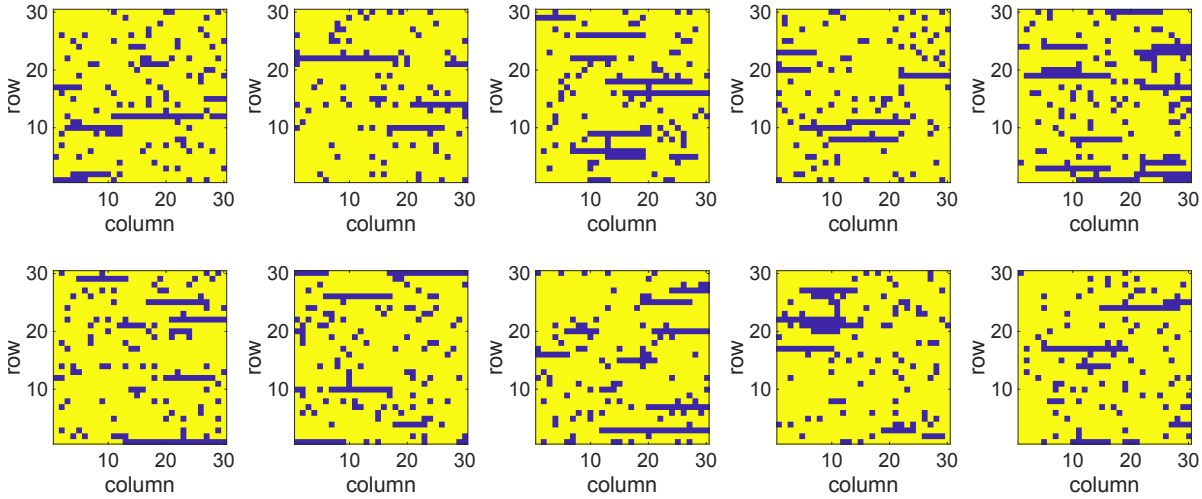

Fig. 5.3: The ten used realizations of the 31-by-31 normalized conductivity pattern for the cells in data set S3.

The concept of fractionated electrograms was explained in Section 4.3.1: these are signals with more than one significant deflection. In this section, we will define secondary deflections as significant if the value of the derivative is 30% or more of the maximum derivative value of the main deflection.

As we described in 4.1.3, measurement noise is included in the simulated data by adding Gaussian-noise terms to the simulated electrograms. In sections 5.2 and 5.3, the noise level of the simulated data is set such that the SNR equals 10 dB.

5.2. Single-wavefront performance

The first setting we consider is that of tissue stimulated from a single point, as illustrated by Fig. 4.2a. Using the conductivity realizations described in Section 5.1, we compare the performance in LAT estimation of five methods. These methods can be subdivided into two groups: three methods are applied directly to the measured electrograms, and two methods are applied on transmembrane currents obtained after deconvolution. In the former group, we have steepest deflection (SD_Φ), normalized cross-correlation (NCC_Φ), and normalized cross-correlation of the derivative (NDCC_Φ). In the latter group, applied to the currents, we have steepest deflection (SD_I) and normalized cross-correlation of the derivative (NDCC_I). To systematically evaluate the performance, we take the square, 11-by-11 electrode grid graph (as is displayed in Fig. 3.3) as a foundation and take the cross-correlation over an increasing number of hops. Thus, we increase the neighbor order P in the graph $G^{(P)}$ and the associated adjacency matrix $\Xi^{(P)}$. As Section 3.3.2 illustrated, the pairwise time delays obtained by

the cross-correlation operation are converted to LATs using ordinary least-squares estimation.

Fig. 5.4 shows the RMSE of the five methods for set S1, normalized with respect to the RMSE of the SD_Φ method. The common normalization factor applied to all four plots allows us to directly compare the five methods. We can see in Fig. 5.4a that the error of the N(D)CC_Φ method drops clearly below that of SD_Φ when $P > 1$; the fractionated sensors show practically the same behavior, albeit with a slightly higher error. The deconvolved methods shown in Fig. 5.4b also outperform the SD_Φ reference: the deconvolved steepest-deflection equivalent SD_I has a lower error than SD_Φ and $NDCC_I$ benefits from inclusion of higher-order neighbors, too. Looking purely at the fractionated sensors here, we see that both methods, in contrast with their Φ counterparts, show a slight increase in performance compared to the total picture shown on the left. On the whole, $NDCC_I$ is seen to perform approximately equally, but slightly better, than the NCC_Φ method, especially in fractionated signals.

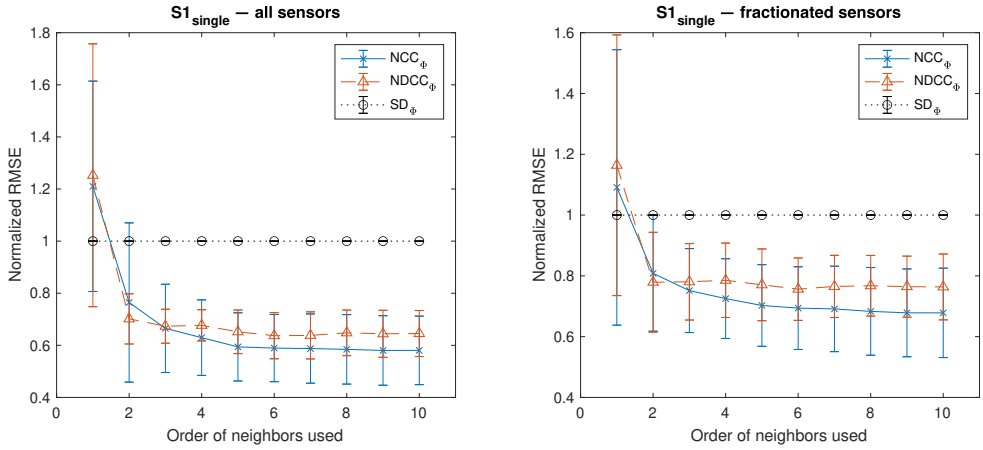

(a)

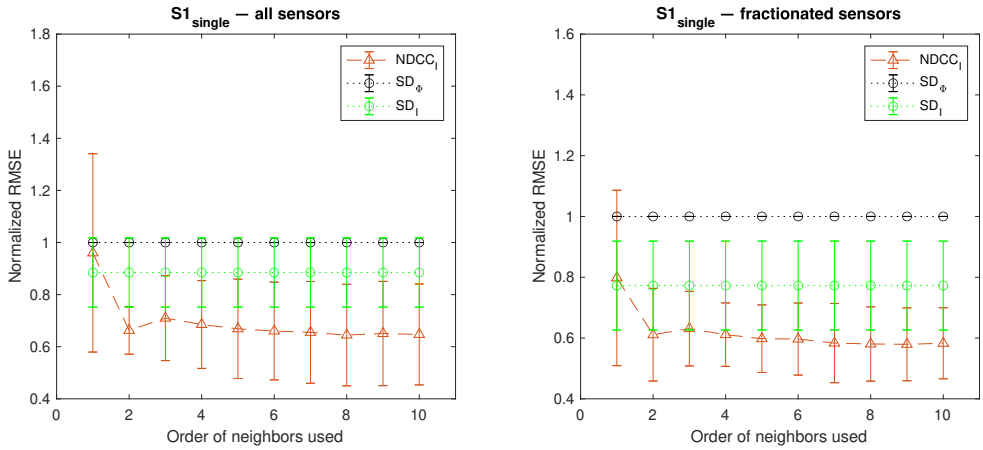

(b)

Fig. 5.4: Normalized RMSE of the estimated LATs, based on the ten realizations of data set S1 with one source. (a) shows the results of directly using the EGMs and (b) shows the results of first applying deconvolution. In the left column, all electrodes are taken into account, while on the right, only electrodes measuring a fractionated signal are considered. The markers correspond to the mean; the bars indicate the standard deviation.

The results for data set S2 are shown in Fig. 5.5. We see similar results here as with S1. The same trend is visible with regard to the error and increasing neighbor order. Once again, the $NDCC_I$ performs better than its electrogram-based counterpart and the performance of both deconvolution-based methods increases when only fractionated sensors are considered. Note, though, that SD_I and $NDCC_I$ show a larger variance in the RMSE compared with the S1 case. This could be related to the fact that the S2 pattern is non-isotropic, resulting in larger differences in wavefront conduction over different realizations of the lines of block.

Fig. 5.6 gives a view of the results for data set S3. Comparable results to S1 and S2 can be

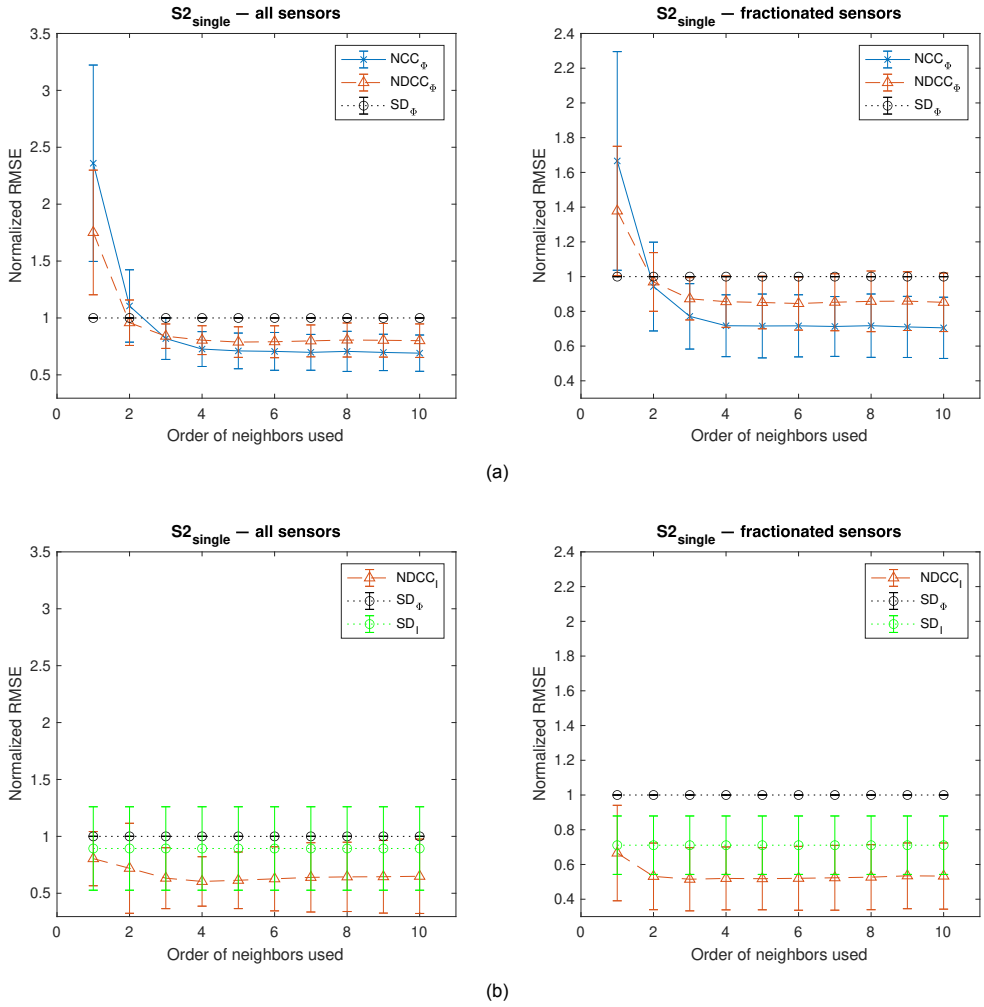

Fig. 5.5: Normalized RMSE of the estimated LATs, based on the ten realizations of data set S2 with one source. (a) shows the results of directly using the EGMs and (b) shows the results of first applying deconvolution. In the left column, all electrodes are taken into account, while on the right, only electrodes measuring a fractionated signal are considered. The markers correspond to the mean; the bars indicate the standard deviation.

observed. A difference is that the error variance in the NDCC$_I$ and SD$_I$ methods has become even larger than was the case for the S2 data set. As the lines of block of S2 are also present in the conductivity pattern of S3, this effect can be partly be explained here in the same way. Furthermore, a larger portion of the simulated tissue now consists of tissue with a low conductivity, making the potential for improvement and the relative differences between multiple realizations (and thus the variance in the error) larger. Specifically for the SD$_I$ method, it should be noted that only one of the ten realizations actually generated a higher RMSE than the SD$_\Phi$ method: this result skewed the mean to a higher value and added to the aforementioned spread in RMSE values we encounter here.

To give an absolute, un-normalized view of the errors, Table 5.1 shows the mean RMSE across the ten realizations of the different tissue types for the five methods. The appended number for the NCC and NDCC methods corresponds to the neighbor order P used to construct the grid graph $G^{(P)}$ and the smallest error for each simulation setting is indicated in bold. The errors for S1 are small for all methods, which can be attributed to the fact that the spots of conduction block impede the activation wave moving through the area only in a limited way. There is limited room for performance, so the spread of errors is relatively small. Both this spread and the error values themselves increase as we look at S2 and S3, which feature higher degrees of conduction block. This then leads to a higher proportion of fractionated electrograms, which can be seen in Table 5.2. Considering all data sets, we can see that NDCC$_I$-10 performs best in all cases when only fractionated sensors are considered, but is slightly outperformed by NCC$_\Phi$-10 in data sets S1 and S3 on the whole. Furthermore, SD$_I$ is seen

to outperform its electrogram-based neighbor SD_Φ, which is in agreement with results found by Abdi *et al.* [19]. In general, the errors of the cross-correlation methods are seen to be inversely related to P, which is congruent to the findings of Kölling *et al.* [21].

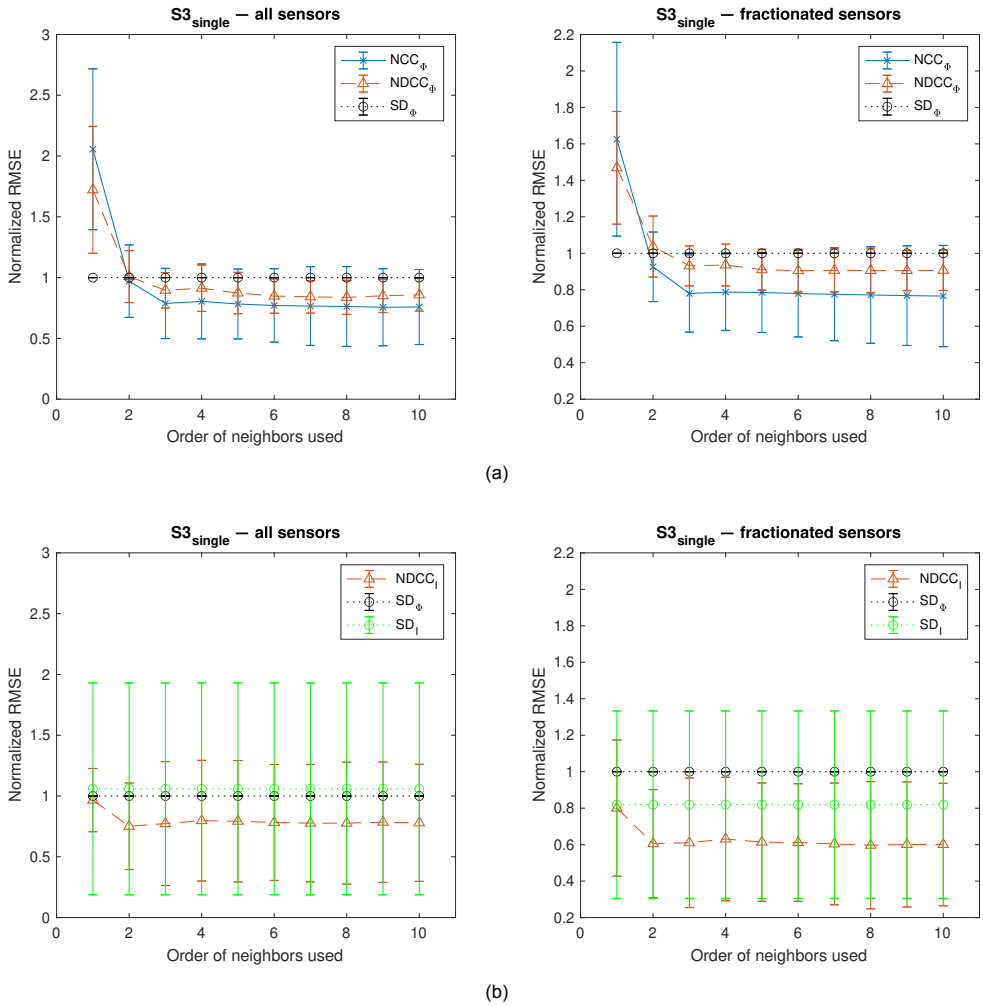

Fig. 5.6: Normalized RMSE of the estimated LATs, based on the ten realizations of data set S3 with one source. (a) shows the results of directly using the EGMs and (b) shows the results of first applying deconvolution. In the left column, all electrodes are taken into account, while on the right, only electrodes measuring a fractionated signal are considered. The markers correspond to the mean; the bars indicate the standard deviation.

Table 5.1: Mean absolute RMSEs in ms for the different LAT estimation methods applied to the ten realizations of the three single-source datasets, using simulated electrograms with an SNR of 10 dB. The three columns on the left take all electrodes into account; in the three on the right (indicated by "(f)"), only electrodes with fractionated signals are included.

	S1	**S2**	**S3**	**S1 (f)**	**S2 (f)**	**S3 (f)**
SD_Φ	0.69	1.28	1.62	1.27	2.72	2.63
NCC_Φ-1	0.81	3.07	3.02	1.27	4.44	4.01
NCC_Φ-10	**0.39**	0.91	**1.05**	0.89	1.95	1.89
NDCC_Φ-1	0.86	2.23	2.42	1.46	3.64	3.65
NDCC_Φ-10	0.44	1.07	1.31	0.99	2.38	2.34
SD_I	0.61	1.10	1.50	0.99	1.99	2.00
NDCC_I-1	0.63	1.11	1.45	0.98	1.94	1.97
NDCC_I-10	0.44	**0.84**	1.16	**0.77**	**1.54**	**1.49**

Table 5.2: Number of irregular signals encountered in the single-source simulations of N = 1210 electrograms with an SNR of 10 dB.

	S1	S2	S3
Inactive electrodes	1	8	28
Fractionated electrograms	64	177	224

5.3. Triple-wavefront performance

Apart from electrical stimulation by one source, Section 4.1.2 described another way to initiate the spreading of action potentials across cardiac tissue. Depicted by Fig. 4.2b, we now position three sources of electrical stimulation at the edges of the measurement area on the simulated atrial tissue. In this way, we can investigate the effect of multiple propagating wavefronts on the estimation of LATs. As in the single-source case described in Section 5.2, we use the thirty conductivity patterns of S1, S2, and S3 described in Section 5.1. The same five LAT estimation methods are considered: SD_Φ, NCC_Φ, $NDCC_\Phi$, SD_I, and $NDCC_I$.

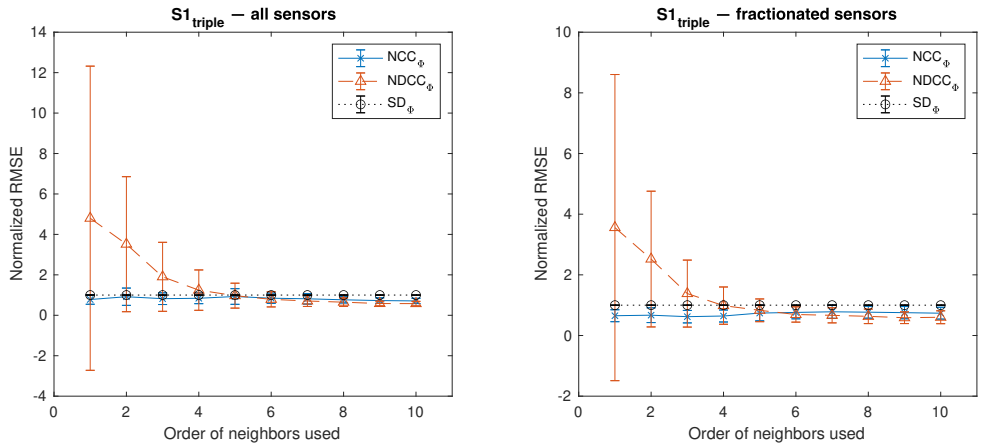

(a)

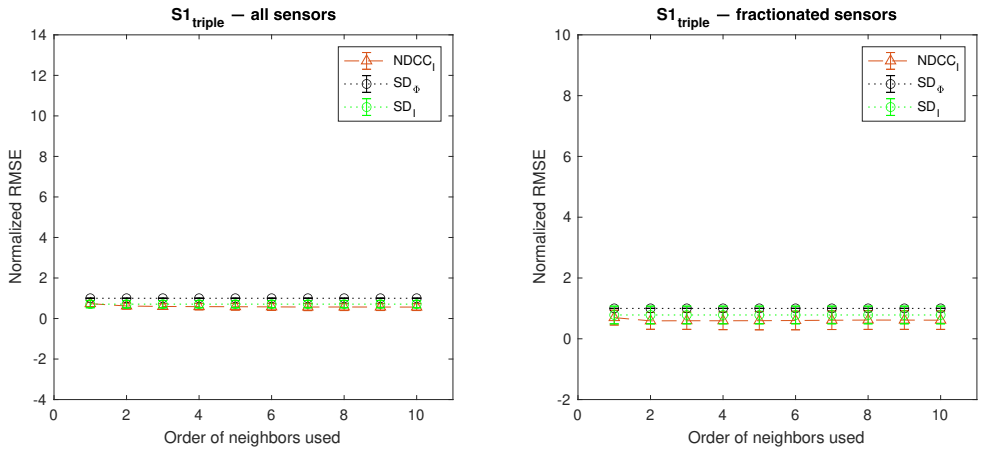

(b)

Fig. 5.7: Normalized RMSE of the estimated LATs, based on the ten realizations of data set S1 with three sources. (a) shows the results of directly using the EGMs and (b) shows the results of first applying deconvolution. In the left column, all electrodes are taken into account, while on the right, only electrodes measuring a fractionated signal are considered. The markers correspond to the mean; the bars indicate the standard deviation.

The RMSE for the aforementioned methods for data set S1, again normalized with respect to the SD_Φ error, are shown in Fig. 5.7; Fig. 5.8 is a zoomed-in version of Fig. 5.7. Across all plots, it can be seen that the SD_Φ reference is outperformed by the other methods. For the two NDCC methods, the error decreases as the neighbor order increases. For the electrogram-based methods, we can see that they outperform the SD_Φ reference, but not as easily as in the single-source case. $NDCC_\Phi$ requires a relatively large amount of information to achieve its best results, with the error only dipping below that of SD_Φ for neighbor order $P > 4$. The RMSE of NCC_Φ fluctuates before decreasing for $P > 5$ on the whole and even slightly increases for the fractionated signals. These observations, along with the relatively large variance of the $NDCC_\Phi$ error for lower P, show that the electrogram-based methods are less consistent when more wave sources are introduced. The $NDCC_I$ and SD_I methods, on the other hand, perform similarly to what was encountered in the single-source case. Note, however, that both NDCC methods eventually reach approximately the same error value for $P = 10$.

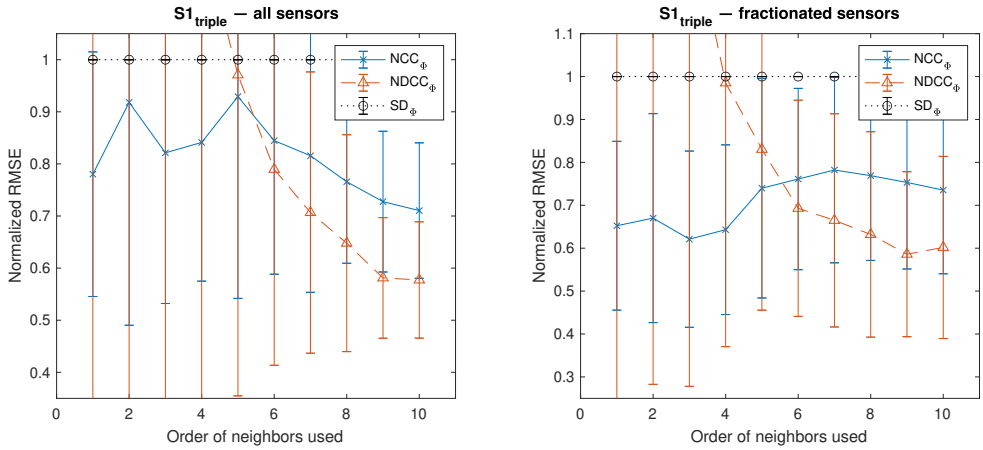

(a)

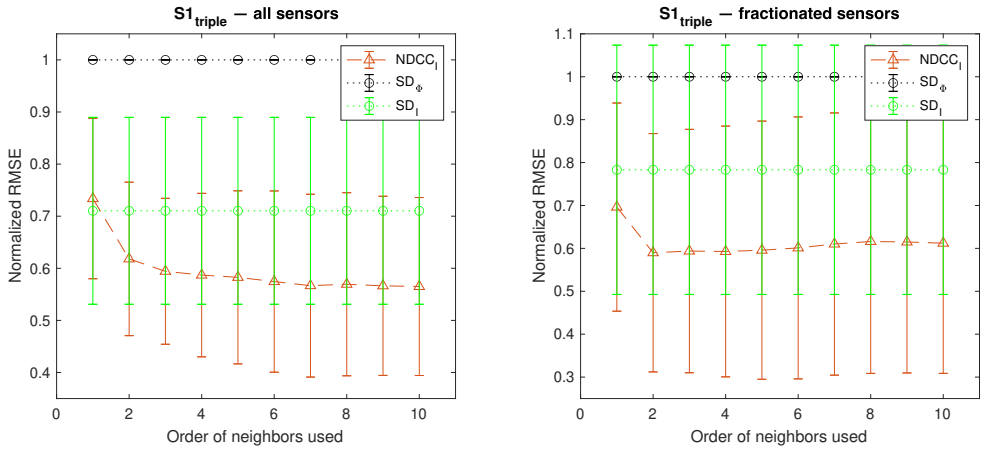

(b)

Fig. 5.8: Vertically zoomed-in version of the normalized RMSEs shown in Fig. 5.7.

The results for the realizations of data set S2 can be seen in Fig. 5.9, with Fig. 5.10 providing a vertically enlarged view of the errors. These N(D)CC$_\Phi$ methods approximately show errors decreasing with P; the error of NDCC$_\Phi$, however, does so in a less steady way, with, again, large variance for lower orders. The deconvolution-based methods perform similarly to the S1 case, with the NDCC$_I$ error dropping steadily, ending up with an error lower than that of NDCC$_\Phi$ (with all methods beating SD$_\Phi$ in terms of the RMSE).

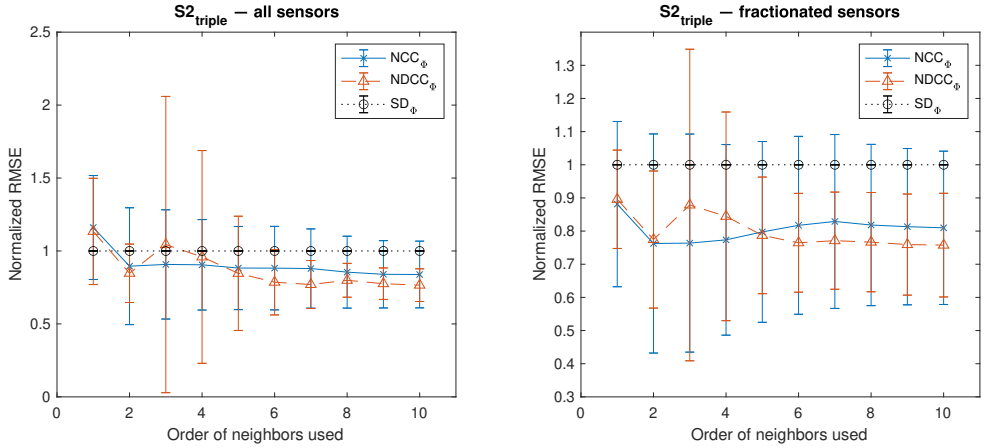

(a)

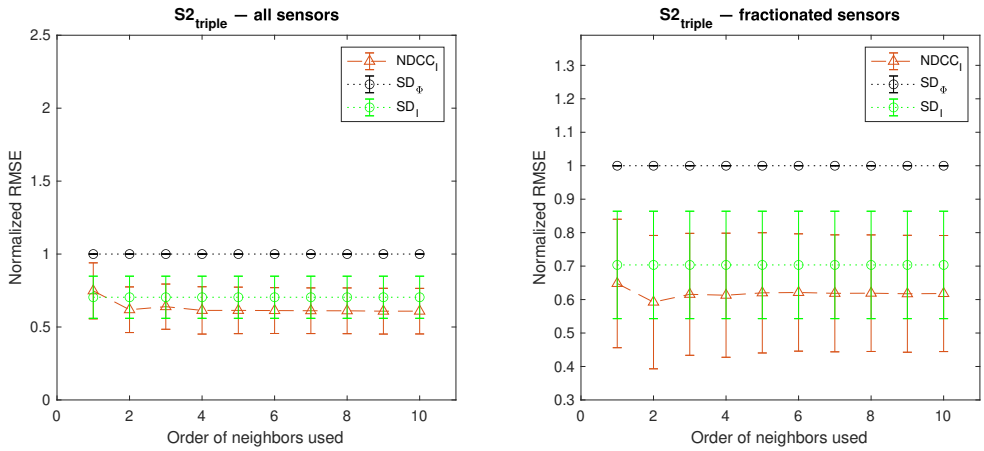

(b)

Fig. 5.9: Normalized RMSE of the estimated LATs, based on the ten realizations of data set S2 with three sources. (a) shows the results of directly using the EGMs and (b) shows the results of first applying deconvolution. In the left column, all electrodes are taken into account, while on the right, only electrodes measuring a fractionated signal are considered. The markers correspond to the mean; the bars indicate the standard deviation.

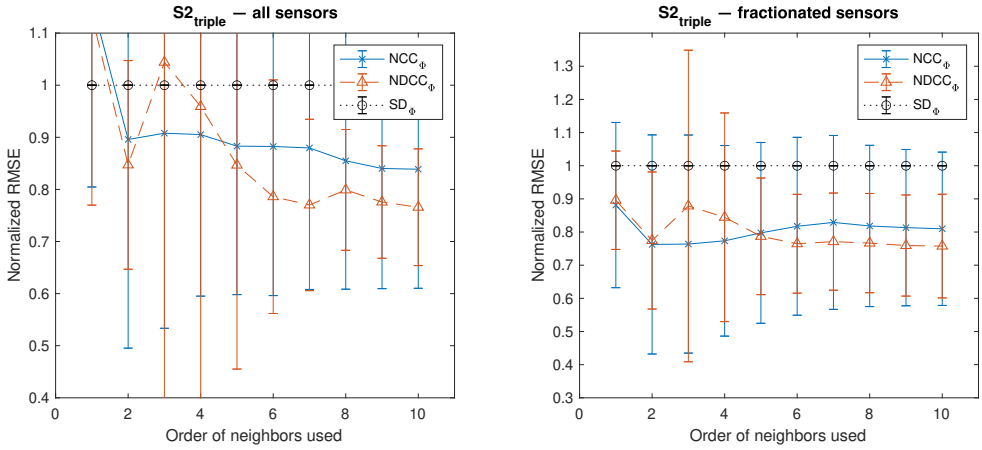

(a)

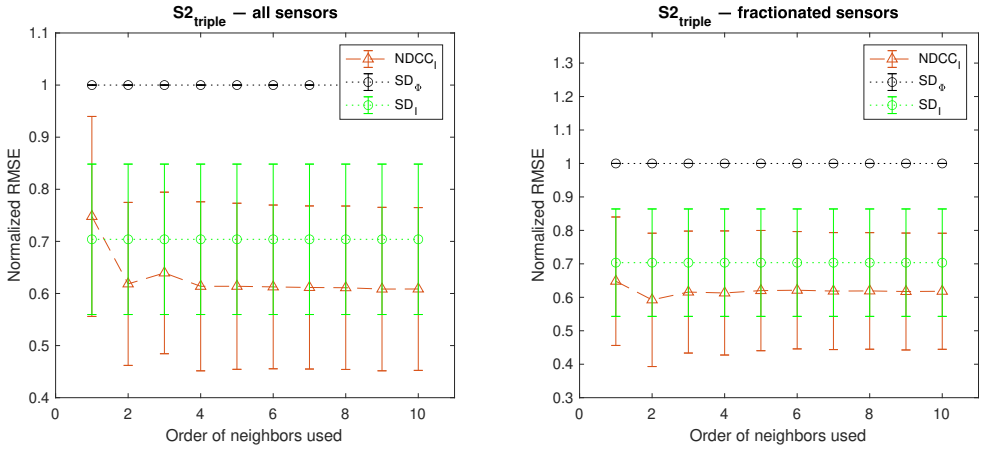

(b)

Fig. 5.10: Vertically zoomed-in version of the normalized RMSEs shown in Fig. 5.9.

Fig. 5.11 shows the results for data set S3, with Fig. 5.12 providing a closer look. We can again recognize the steadily decreasing error across all cross-correlation methods. However, the combination of a large area of conduction block and more stimulation sources here provides for a complex setting, which causes relative difficulties for the estimation algorithms. All methods exhibit variances that are much larger than was the case for S1 and S2. The NCC_Φ method does not manage to outperform the SD_Φ reference this time and $NDCC_\Phi$ shows a large spread of errors across the neighbor orders. In comparison, the deconvolution-based methods are relatively consistent in beating the RMSE of SD_Φ, with $NDCC_I$ again achieving the lowest RMSE of the methods considered.

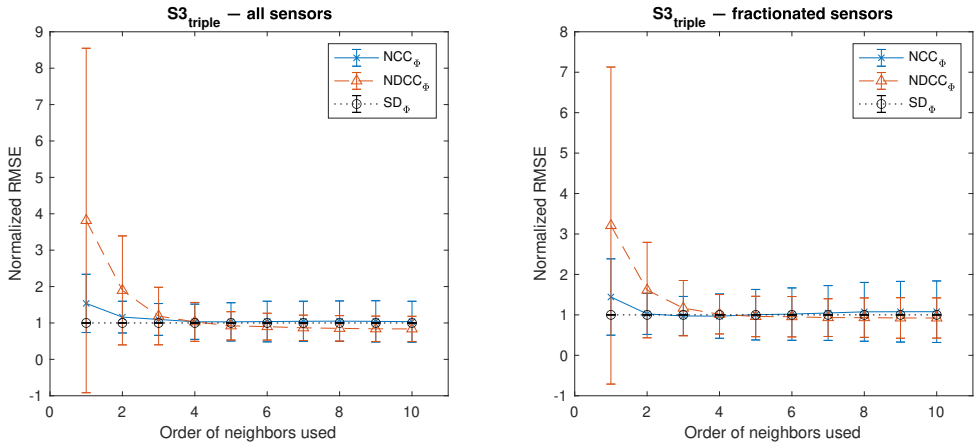

(a)

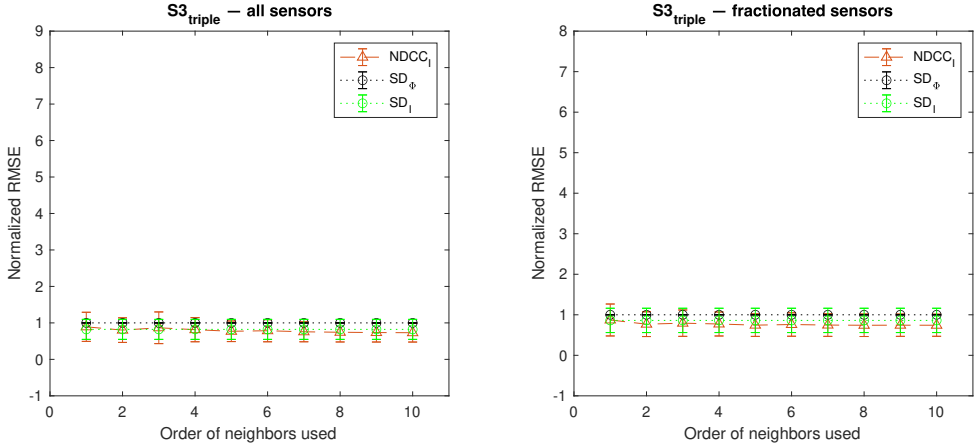

(b)

Fig. 5.11: Normalized RMSE of the estimated LATs, based on the ten realizations of data set S3 with three sources. (a) shows the results of directly using the EGMs and (b) shows the results of first applying deconvolution. In the left column, all electrodes are taken into account, while on the right, only electrodes measuring a fractionated signal are considered. The markers correspond to the mean; the bars indicate the standard deviation.

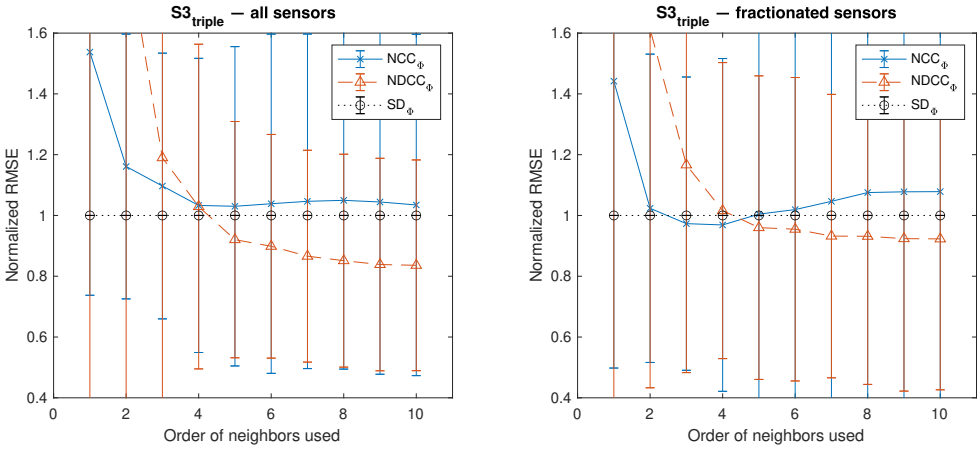

(a)

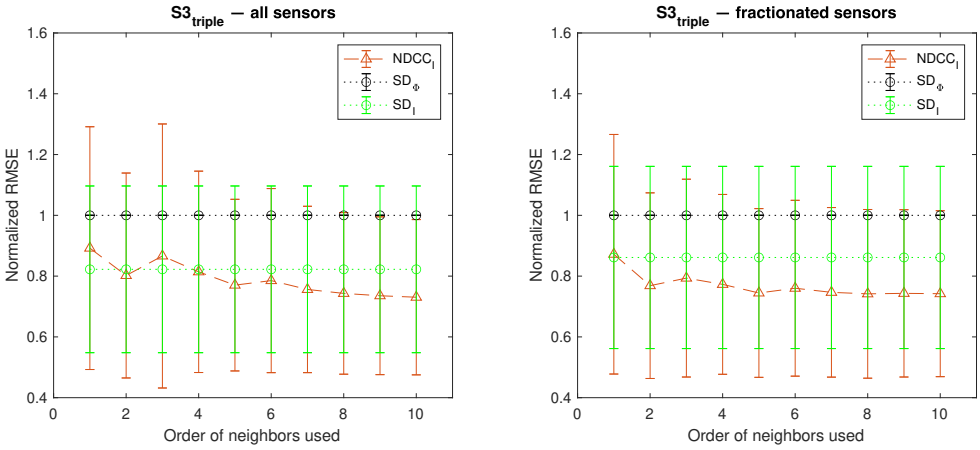

(b)

Fig. 5.12: Vertically zoomed-in version of the normalized RMSEs shown in Fig. 5.11.

The mean of the absolute errors for the simulation settings considered in this section are shown in Table 5.3. Some trends that were encountered in the single-source case show up here as well, like the increasing error across the board as data sets S1, S2, and S3 are considered; SD_I performing better than SD_Φ; and the cross-correlation error generally decreasing for higher neighbor order. Except for the fractionated sensors in data set S1, where $NDCC_\Phi$-10 beats it slightly, we can see that the $NDCC_I$-10 method, again, has the lowest RMSE in this simulation. There are also differences with the single-source errors in Table 5.1. Overall, the errors in the triple-source case are larger, due to the increased complexity of the simulation setting, resulting in a larger number of fractionated electrograms, which is apparent from Table 5.4.

Table 5.3: Mean absolute RMSEs in ms for the different LAT estimation methods applied to the ten realizations of the three triple-source datasets, using simulated electrograms with an SNR of 10 dB. The three columns on the left take all electrodes into account; in the three on the right (indicated by "(f)"), only electrodes with fractionated signals are included.

	S1	**S2**	**S3**	**S1 (f)**	**S2 (f)**	**S3 (f)**
SD_Φ	1.13	1.66	1.83	1.62	3.03	2.77
NCC_Φ-1	0.87	1.95	2.60	1.04	2.71	3.33
NCC_Φ-10	0.80	1.40	1.71	1.19	2.46	2.51
$NDCC_\Phi$-1	5.97	1.91	5.27	6.57	2.73	5.91
$NDCC_\Phi$-10	0.65	1.28	1.41	**0.98**	2.27	2.19
SD_I	0.80	1.18	1.47	1.27	2.15	2.26
$NDCC_I$-1	0.83	1.25	1.59	1.13	1.96	2.28
$NDCC_I$-10	**0.64**	**1.01**	**1.31**	1.01	**1.86**	**1.98**

Table 5.4: Number of irregular signals encountered in the triple-source simulations of N = 1210 electrograms with an SNR of 10 dB.

	S1	**S2**	**S3**
Unactive electrodes	1	8	28
Fractionated electrograms	291	300	434

In the end, the main observation that can be made about the proposed algorithm of combining deconvolution and cross-correlation ($NDCC_I$) is not necessarily the low error (which often differs from $NDCC_\Phi$ only by a small amount), but the higher degree of consistency and robustness it shows. This may not be as visible in Table 5.3, but was noted primarily in Fig. 5.7 to Fig. 5.11. This aspect of the fact can be explained by remembering a key feature of the deconvolution algorithm, mentioned in Section 3.2. In the currents this operation produces, local activity is amplified, while distant contributions are attenuated. This makes this modality better suited to handle situations with spatially fast-changing properties, such as those with large areas of block and multiple wavefronts, as was simulated in this section. In Fig. 5.7b to Fig. 5.11b, we can see that the main decrease of the error in fractionated signals occurs as P changes from 1 to 2; the error could almost be said to saturate. This fits the idea that the used signals are now more local, so cross-correlating them with their relatively close-by neighbors has the biggest impact on the accuracy of the obtained delays and thus the LATs.

5.4. Impact of noise

In the previous sections, the behavior of the various LAT estimation methods was investigated in a number of different simulated tissue settings, varying in the type of conduction block and the number of simulated wavefronts. As we generated the simulation data ourselves, we had the advantage of being able to specify the amount of noise present in the signals. All electrograms were simulated with noise, corresponding to an SNR of 10 dB. To find out how much of an impact the modeled measurement noise has on the estimation of activation times, it can be interesting to vary this amount. In Section 4.1.3, some examples were given of electrograms with increasing levels of noise. In keeping with the signals shown there in Fig. 4.6, we consider four values for the SNR: 0, 10, 20, and 50 dB (where the noise level is negligible). The ten realizations of conductivity pattern S3 are then used to generate simulated

electrograms, to which the five LAT estimation methods are applied. For the cross-correlation methods, their lag-10 ($P = 10$) versions are used. This results in a view of the course of the RMSE as the noise contribution becomes increasingly stronger.

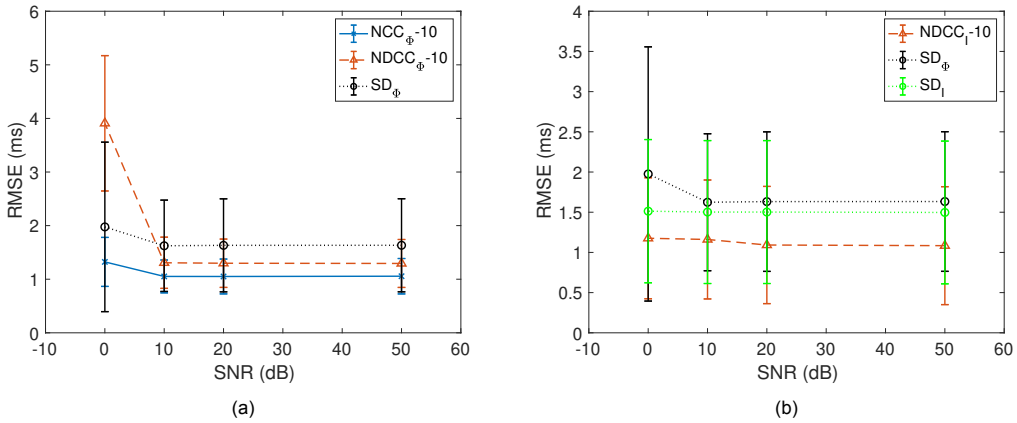

Fig. 5.13: RMSEs of the five LAT estimation methods for different noise levels, using the ten single-source realizations of data set S3. The markers indicate the mean values; the vertical bars indicate the standard deviation.

First, we consider the single-source version of S3 (see also Fig. 4.2a). The resulting errors can be seen in Fig. 5.13. The electrogram-based methods are shown on the left; the plot on the right shows the deconvolution-based methods, along with SD$_\Phi$ as a reference. What is surprising to see in Fig. 5.13a, is that the errors stay approximately constant, until the SNR reaches 0 dB. In this setting, with equal noise and signal power, the error is still only slightly increased (except for the NDCC$_\Phi$ method, which shows a larger increment). Also noticeable is the larger variance that both NDCC$_\Phi$ and SD$_\Phi$ have at this noise level. The deconvolution-based methods in Fig. 5.13b have practically the same mean error and variance across all SNR values, showing remarkably stable performance.

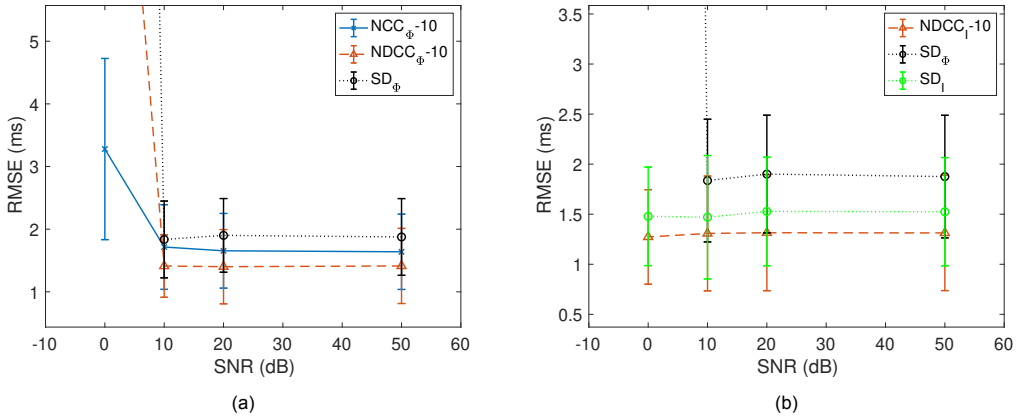

Fig. 5.14: RMSEs of the five LAT estimation methods for different noise levels, using the ten triple-source realizations of data set S3. The markers indicate the mean values; the vertical bars indicate the standard deviation.

Next, we use the same conductivity pattern of S3, but now with the relatively more complex triple-source stimulation setting (see also Fig. 4.2b). Fig. 5.14 shows the results; a zoomed-out view of the electrogram-based errors is given by Fig. 5.15. Down to 10 dB, the errors again stay approximately level. In Fig. 5.14a, we also see the errors (and the variance) increase at 0 dB as we saw before, but now in a much more drastic way. With a waveform like in Fig. 4.6d, the time derivative of the electrogram is no longer reliable for LAT estimation, as the noise deflections are relatively large. A noticeable peak (corresponding to activation) still remains in the electrogram, which explains why NCC$_\Phi$ doesn't suffer as big a performance drop. The transmembrane-current-based methods shown in Fig. 5.14b remarkably enough show virtually the same results as in the single-source case, with the error even

fractionally decreasing at the highest level of noise.

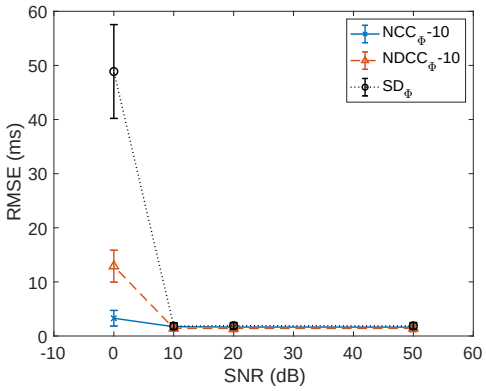

Fig. 5.15: Vertically zoomed-out version of Fig. 5.14a.

With these results, some conclusions about the impact of additive noise on the performance of the LAT estimation methods can be made. In general, all methods cope well with noise levels of up to an equivalent 10-dB SNR. There seems to be no difference in performance in lower noise levels. This could be related to the fact that the part of the measured data that we are interested in, the actual atrial activity, is relatively sparse in the temporal domain. It is zero most of the time, with one (or more) relatively sharp, large deflections. This makes it stand out in the signal, even when the SNR is relatively low. Therefore, for the noise to have a negative impact in locating the activation time, the noise level has to be high—0 dB, as Fig. 5.13 and Fig. 5.14 showed. However, in deviation from this trend, the deconvolution based methods do not seem to be affected at all by the levels of noise we investigated. An explanation for this could lie in the way the equivalent transmembrane currents are generated by the deconvolution algorithm. As we saw in Section 3.2, this quantity results from solving the inverse problem (3.7), made feasible by adding a regularization term incorporating prior knowledge. This term promotes sparsity in the time derivative of the currents. A consequence of this is that the noise present in the input electrograms is effectively attenuated in the output I', thus making the SD$_I$ and NDCC$_I$ methods more robust against higher levels of noise.

6

Conclusions

6.1. Summary of results

In this thesis, we investigated the merits of combining two existing methods for processing voltage data obtained by epicardial electrode array on the atria to improve the annotation of the local activation times at the electrode locations. The epicardial signals formed the basis for an inverse problem, which was solved to recover underlying quantities responsible for the measured signals. Cross-correlation was then applied to these underlying signals over pairs of electrodes, for directly neighboring points and higher-order neighbors. Local activation times resulted through processing of the pairwise delays thus obtained; the performance in this regard was compared to existing methods.

Chapter 2 provided some background information on the topic at hand. The anatomy of the heart and conduction of electrical signals in the atria was illustrated, leading to a model of the action potential that is responsible for contraction of cardiac cells. Different ways of quantifying this electrical activity were shown, culminating in a model of cell-level currents responsible for the electrograms measured at epicardial level with an electrode array. Using this modality, various existing methods were described to extract the time of activation of cardiac tissue underneath the measuring electrode.

Using this understanding of atrial electrical activity, a two-part algorithm was proposed in Chapter 3 to improve on the estimation of activation by exploiting spatial information in the recorded data. A model for electrograms was provided, modeling them as a sum of a main deflection of interest and secondary disturbances. As these disturbances can impair the performance of cross-correlation methods in settings of impaired atrial electrical conductivity, an extra constituent method was introduced. This solves an inverse problem to obtain from the measured electrograms the underlying transmembrane currents, which were shown to give a more local view of atrial activity. This was then passed to the next part of the algorithm, the basis of which was formed by spatially defining the measuring electrode array as a grid graph. For pairs of electrodes in this graph, the corresponding currents obtained in the previous step were cross-correlated. Doing this not only for direct neighbors, but also for points with more hops in between, provided an estimate for the mutual time delays of activation. From these delays, the absolute activation times could then be obtained through least-squares processing.

In Chapter 4, a number of methods were discussed that could be used to simulate the electrical activity in a two-dimensional piece of atrial tissue. Models for three different types of blocks in conduction typical of atrial tissue were presented, along with two different ways in which the stimulation of the atrial tissue could be modeled. This provided a data set of 7260 electrograms from a simulated electrode array of 121 electrodes.

Chapter 5 described how the proposed methodology was tested experimentally with the described simulation data to evaluate its performance. A number of different methods were used in simulated settings of varying complexity. This produced quantitative results with which some comparisons could be made.

First, the proposed method of cross-correlation of the current over higher-order neighbors was applied to a setting with one source of electrical activity, along with (regular) cross-correlation of the electrograms over higher-order neighbors, steepest deflection of the electrogram (used as a baseline), and steepest deflection the current. Results found in [19] and [76] were confirmed, with the steepest

deflection showing better results applied to the current than to the electrogram and the performance of the cross-correlation methods increasing as the used neighbor order increased. The proposed cross-correlation of the current slightly outperformed the regular cross-correlation methods.

The methods were then tested on data sets with three sources of electrical stimulation. In this more elaborate setting with more wavefront conflicts, the regular cross-correlation methods were shown to experience more difficulty. Their performance fluctuated, and in some cases only performed similarly to the baseline method of steepest deflection of the electrogram. The cross-correlation of the current, though having similar errors to the electrogram-based methods in a number of situations, showed an increase in performance in the situations where the regular cross-correlation methods struggled most. Yet, the primary takeaway in this setting is the more consistent, less-varying performance of the transmembrane-current method as the amount of hops involved in the cross-correlation was made greater.

Finally, the impact of different noise levels was studied, which, somewhat surprisingly, showed a relative tolerance of all methods to noise until very low SNR levels were reached. However, for data sets with multiple stimulations, the deterioration in performance at these high-noise levels became more dramatic in the reference methods. In spite of that, the proposed method proved, remarkably, to give stable performance even in the aforementioned highly noisy settings; this was postulated to be related to the way prior knowledge was included in the solution of the inverse problem that provides the basis for the transmembrane currents on which the method acts.

With regard to the methodology proposed in this thesis, which was detailed in Chapter 3, we can conclude, based on the simulated results of Chapter 5, that its merits are primarily to be found in the form of increased consistency, not necessarily improving accuracy of existing methods.

6.2. Future work

The work done for this thesis makes a humble foray into the field of research on heart arrhythmias and quantifying cardiac electrical activity. A number of assumptions and simplifications of reality have been done and subjects prioritized, that suggest more research that can be done on a number of different topics.

6.2.1. Clinical validation

The results in this thesis were obtained based on simulated data; it would be valuable to verify the findings presented here on real-world clinical data of atrial electrical activity. The simulated results seem to suggest that the proposed method has a larger potential for improvement in cardiac settings of relatively high complexity. Clinical data will produce more varied signals, with possibly more complex morphologies and settings of wavefronts and conduction block that are more involved than what our simulation model can provide. It would therefore be interesting to validate this trend and see how the deconvolution–cross-correlation combination performs there.

6.2.2. Modeling of cardiac tissue

In this work, the electrode array with which measurements were done was assumed to be positioned at a constant height parallel to the cardiac tissue, which was modeled as a plane. This naturally is a simplification of reality, as myocardium is a three-dimensional object, which we projected onto two dimensions. Furthermore, a planar representation disregards the curvature of the tissue and spots were the electrical contact of the electrode array and the tissue could be impaired. Some features are thus lost in the model. With studies showing that the depth direction can show a marked variety (so-called *asynchrony*) in electrical activity across different layers of cardiac cells [38]–[41], adapting the used tissue model could be beneficial in providing more understanding of the atrial activity.

6.2.3. Spatial connection between deconvolution and cross-correlation

The connection and interplay between the deconvolution and cross-correlation algorithms could be investigated further. Both methods employ spatial information present in the way the electrograms are measured, but each in a different fashion. Seeing how and where this spatial connection influences the obtained results could provide valuable insight. For example, the deconvolution algorithm models the electrograms as spatial averages of the transmembrane currents in the surrounding cells. In implementing this algorithm, the spatial support needs to be defined for the distance kernel effecting

this averaging. This thus determines the neighbor order of electrodes contributing to the electrogram measured in a given location; the question that arises is whether this number also shows up when evaluating LAT estimation results for different neighbor orders of the cross-correlation method.

6.2.4. Benchmarking deconvolution

The deconvolution method used in this work was originally derived with a relatively specific purpose in mind: accuracy of the first-order time derivative of the resulting transmembrane current. Interpreting the output currents of this algorithm provides us with a difficulty, as, in contrast with the electrogram (of which many thorough theoretical and practical analyses exist in literature), these currents are a quantity that cannot be readily validated with real-life measurements. It would be worthwhile to look into a way in which a better sense of real-world transmembrane currents could be obtained, such that the accuracy of a deconvolution method such as the one used in this work could be benchmarked.

6.2.5. Wavefront dynamics

The aspect of multiple wavefronts in a measurement area could also benefit from more detailed study. This thesis incorporated this aspect into the simulation data, but in a somewhat limited way. In the case of multiple stimulation sources, the time or instance of activation was equal across the sources. It could be interesting to investigate the effects of non-simultaneous stimulation of atrial tissue. Additionally, a question that arises when considering such a setting is whether electrograms measured in the vicinity of a stimulation source could benefit from being considered separately from those close to another source. If this course of action has merit, a number of existing algorithms could be explored with which activation wavefronts can be tracked through space and time, such as [85], [86].

6.2.6. Modeling of measurement noise

The simulated data used in this work includes a term to incorporate noise that may be present in measured signals in a clinical setting. This measurement noise was modeled as additive white Gaussian noise, primarily out of convenience in processing. The accuracy of this part of the model with respect to real-world noise terms was not explicitly considered and could therefore be investigated further.

References

[1] W. Fontein, “De electrotechniek,” in *De Technische Hogeschool te Delft 1905–1955*, A. F. Kamp, Ed., The Hague, The Netherlands: Staatsdrukkerij- en Uitgeverijbedrijf, 1955, pp. 237–245.

[2] H. Baudet, *De lange weg naar de Technische Universiteit Delft: De Delftse ingenieursschool en haar voorgeschiedenis*. The Hague, The Netherlands: SDU, 1992, ISBN: 978-90-12-06590-9.

[3] J. Davidse, *Spanning: Geschiedenis van de Delftse opleiding tot elektrotechnisch ingenieur*, E. Backer, H. B. Verbruggen, J. Kapteijn, W. H. van ’t Hoogerhuijs, and J. M. Brans, Eds. Delft, The Netherlands: Delft Univ. Press, 1998, ISBN: 90-407-1794-X. [Online]. Available: http://resolver.tudelft.nl/uuid:1fa4d45b-5b13-4965-ad7a-ca5d1fa97db5.

[4] “Cardiovascular diseases (CVDs),” World Health Organization. (Jun. 11, 2021), [Online]. Available: https://www.who.int/en/news-room/fact-sheets/detail/cardiovascular-diseases-(cvds) (accessed Aug. 4, 2022).

[5] E. Wilkins *et al.*, “European cardiovascular disease statistics 2017,” Eur. Heart Netw., Brussels, Belgium, Rep. 2017. [Online]. Available: https://ehnheart.org/images/CVD-statistics-report-August-2017.pdf.

[6] D. Mozaffarian *et al.*, “Executive summary: Heart disease and stroke statistics—2016 update. A report from the American Heart Association,” *Circulation*, vol. 133, no. 4, pp. 447–454, Jan. 2016. DOI: 10.1161/CIR.0000000000000366.

[7] N. M. S. de Groot. “Met de hand op het hartritme.” (2019), [Online]. Available: http://hdl.handle.net/1765/123976.

[8] A. D. Krahn, J. Manfreda, R. B. Tate, F. A. L. Mathewson, and T. E. Cuddy, “The natural history of atrial fibrillation: Incidence, risk factors, and prognosis in the Manitoba Follow-Up Study,” *Am. J. Med.*, vol. 98, no. 5, pp. 476–484, May 1995. DOI: 10.1016/S0002-9343(99)80348-9.

[9] M. K. Chung *et al.*, “Lifestyle and risk factor modification for reduction of atrial fibrillation: A scientific statement from the American Heart Association,” *Circulation*, vol. 141, no. 16, pp. E750–E772, Apr. 2020. DOI: 10.1161/CIR.0000000000000748.

[10] A. D. Ceornodolea, R. Bal, and J. L. Severens, “Epidemiology and management of atrial fibrillation and stroke: Review of data from four European countries,” *Stroke Res. Treat.*, vol. 2017, May 2017. DOI: 10.1155/2017/8593207.

[11] S. Stewart, C. L. Hart, D. J. Hole, and J. J. V. McMurray, “Population prevalence, incidence, and predictors of atrial fibrillation in the Renfrew/Paisley study,” *Heart*, vol. 86, no. 5, pp. 516–521, Nov. 2001. DOI: 10.1136/HEART.86.5.516.

[12] H. Calkins *et al.*, “2017 HRS/EHRA/ECAS/APHRS/SOLAECE expert consensus statement on catheter and surgical ablation of atrial fibrillation,” *Europace*, vol. 20, no. 1, pp. e1–e160, Jan. 2018. DOI: 10.1093/EUROPACE/EUX274.

[13] W. Einthoven, “Ueber die Form des menschlichen Electrocardiogramms,” *Pflügers Arch. gesamte Physiol. Menschen Tiere*, vol. 60, no. 3-4, pp. 101–123, Mar. 1895. DOI: 10.1007/BF01662582.

[14] W. Einthoven, “Galvanometrische registratie van het menschelijk electrocardiogram,” in *Herinneringsbundel professor S.S. Rosenstein bij gelegenheid van zijn aftreden als hoogleeraar aangeboden door dankbare leerlingen en vrienden*, Leiden, The Netherlands: Eduard IJdo, 1902, ch. 9, pp. 101–106.

[15] W. B. Fye, “A history of the origin, evolution, and impact of electrocardiography,” *Am. J. Cardiol.*, vol. 73, no. 13, pp. 937–949, May 1994. DOI: 10.1016/0002-9149(94)90135-X.

[16] A. Yaksh *et al.*, “A novel intra-operative, high-resolution atrial mapping approach,” *J. Interv. Card. Electrophysiol.*, vol. 44, no. 3, pp. 221–225, Oct. 2015. DOI: 10.1007/S10840-015-0061-X.

[17] C. D. Cantwell, C. H. Roney, F. S. Ng, J. H. Siggers, S. J. Sherwin, and N. S. Peters, “Techniques for automated local activation time annotation and conduction velocity estimation in cardiac mapping,” *Comput. Biol. Med.*, vol. 65, pp. 229–242, Oct. 2015. DOI: 10.1016/j.compbiomed.2015.04.027.

[18] M. S. Spach and P. C. Dolber, “Relating extracellular potentials and their derivatives to anisotropic propagation at a microscopic level in human cardiac muscle. Evidence for electrical uncoupling of side-to-side fiber connections with increasing age,” *Circ. Res.*, vol. 58, no. 3, pp. 356–371, Mar. 1986. DOI: 10.1161/01.RES.58.3.356.

[19] B. Abdi, R. C. Hendriks, A.-J. van der Veen, and N. M. S. de Groot, “Improved local activation time annotation of fractionated atrial electrograms for atrial mapping,” *Comput. Biol. Med.*, vol. 117, pp. 103590:1–103590:12, Feb. 2020. DOI: 10.1016/j.compbiomed.2019.103590.

[20] R. Dubois, S. Labarthe, Y. Coudiere, M. Hocini, and M. Haissaguerre, “Global and directional activation maps for cardiac mapping in electrophysiology,” in *Comput. Cardiol. 2012*, vol. 39, Kraków, Poland, Sep. 9–12, 2012, pp. 349–352.

[21] B. Kölling, B. Abdi, N. M. S. de Groot, and R. C. Hendriks, “Local activation time estimation in atrial electrograms using cross-correlation over higher-order neighbors,” in *Proc. 28th Eur. Signal Process. Conf. (EUSIPCO 2020)*, Amsterdam, The Netherlands, Jan. 18–21, 2021, pp. 905–909. DOI: 10.23919/Eusipco47968.2020.9287434.

[22] D. E. L. Wilcken, “Physiology of the normal heart,” *Surgery*, vol. 36, no. 2, pp. 48–51, Feb. 2018. DOI: 10.1016/j.mpsur.2017.11.009.

[23] *Anatomy and Physiology*. Houston, TX, USA: OpenStax, 2017, ISBN: 978-1-938168-13-0. [Online]. Available: https://openstax.org/details/books/anatomy-and-physiology.

[24] I. Kotadia *et al.*, “Anisotropic cardiac conduction,” *Arrhythmia Electrophysiol. Rev.*, vol. 9, no. 4, pp. 202–210, Dec. 2020. DOI: 10.15420/AER.2020.04.

[25] N. Jost, “Transmembrane ionic currents underlying cardiac action potential in mammalian hearts,” in *Advances in Cardiomyocyte Research*, P. P. Nánási, Ed., 1st ed., Kerala, India: Transworld Research Network, 2009, ch. 1, pp. 1–45, ISBN: 978-81-7895-418-9.

[26] P. W. Macfarlane, A. van Oosterom, O. Pahlm, P. Kligfield, M. Janse, and J. Camm, Eds., *Comprehensive Electrocardiology*, 2nd ed. London, U.K.: Springer-Verlag, 2011, vol. 1. DOI: 10.1007/978-1-84882-046-3.

[27] “Cardiac arrhythmias,” TextbookofCardiology.org. (Dec. 28, 2011), [Online]. Available: https://textbookofcardiology.org/wiki/Cardiac_Arrhythmias (accessed Jul. 28, 2022).

[28] N. Virag *et al.*, “Study of atrial arrhythmias in a computer model based on magnetic resonance images of human atria,” *Chaos*, vol. 12, no. 3, pp. 754–763, Sep. 2002. DOI: 10.1063/1.1483935.

[29] M. Courtemanche, R. J. Ramirez, and S. Nattel, “Ionic mechanisms underlying human atrial action potential properties: Insights from a mathematical model,” *Am. J. Physiol. Heart Circ. Physiol.*, vol. 275, no. 1, pp. H301–H321, Jul. 1998. DOI: 10.1152/ajpheart.1998.275.1.h301.

[30] A. Bardai, M. T. Blom, D. A. van Hoeijen, H. W. M. van Deutekom, H. J. Brouwer, and H. L. Tan, “Atrial fibrillation is an independent risk factor for ventricular fibrillation: A large-scale population-based case-control study,” *Circ. Arrhythmia Electrophysiol.*, vol. 7, no. 6, pp. 1033–1039, Dec. 2014. DOI: 10.1161/CIRCEP.114.002094.

[31] M. M. Gallagher and J. Camm, “Classification of atrial fibrillation,” *Am. J. Cardiol.*, vol. 82, no. 7, pp. 18N–28N, Oct. 1998. DOI: 10.1016/S0002-9149(98)00736-X.

[32] T. Kato, T. Yamashita, K. Sagara, H. Iinuma, and L.-T. Fu, “Progressive nature of paroxysmal atrial fibrillation: Observations from a 14-year follow-up study,” *Circ. J.*, vol. 68, no. 6, pp. 568–572, May 2004. DOI: 10.1253/circj.68.568.

[33] S. Petrutiu, J. Ng, G. M. Nijm, H. Al-Angari, S. Swiryn, and A. V. Sahakian, “Atrial fibrillation and waveform characterization,” *IEEE Eng. Med. Biol. Mag.*, vol. 25, no. 6, pp. 24–30, Nov.–Dec. 2006. DOI: 10.1109/EMB-M.2006.250505.

[34] R. Starreveld-Brand, “Uncovering atrial fibrillation complexity: From signals to (bio)markers,” PhD dissertation, Dept. of Cardiol., Erasmus Univ. Rotterdam, Rotterdam, The Netherlands, 2021. [Online]. Available: http://hdl.handle.net/1765/135378.

[35] G. K. Moe and J. A. Abildskov, “Atrial fibrillation as a self-sustaining arrhythmia independent of focal discharge,” *Am. Heart J.*, vol. 58, no. 1, pp. 59–70, Jul. 1959. DOI: 10.1016/0002-8703(59)90274-1.

[36] G. K. Moe, W. C. Rheinboldt, and J. A. Abildskov, “A computer model of atrial fibrillation,” *Am. Heart J.*, vol. 67, no. 2, pp. 200–220, Feb. 1964. DOI: 10.1016/0002-8703(64)90371-0.

[37] J. W. Waks and M. E. Josephson, “Mechanisms of atrial fibrillation – reentry, rotors and reality,” *Arrhythmia Electrophysiol. Rev.*, vol. 3, no. 2, pp. 90–100, 2014. DOI: 10.1007/BF00502922.

[38] N. M. S. de Groot *et al.*, “Direct proof of endo-epicardial asynchrony of the atrial wall during atrial fibrillation in humans,” *Circ. Arrhythmia Electrophysiol.*, vol. 9, no. 5, May 2016. DOI: 10.1161/CIRCEP.115.003648.

[39] L. J. M. E. van der Does *et al.*, “Unipolar atrial electrogram morphology from an epicardial and endocardial perspective,” *Heart Rhythm*, vol. 15, no. 6, pp. 879–887, Jun. 2018. DOI: 10.1016/j.hrthm.2018.02.020.

[40] B. J. Hansen *et al.*, “Atrial fibrillation driven by micro-anatomic intramural re-entry revealed by simultaneous sub-epicardial and sub-endocardial optical mapping in explanted human hearts,” *Eur. Heart J.*, vol. 36, no. 35, pp. 2390–2401, Sep. 2015. DOI: 10.1093/eurheartj/ehv233.

[41] B. J. Hansen, T. A. Csepe, J. Zhao, A. J. Ignozzi, J. D. Hummel, and V. V. Fedorov, “Maintenance of atrial fibrillation: Are reentrant drivers with spatial stability the key?” *Circ. Arrhythmia Electrophysiol.*, vol. 9, no. 10, pp. 1–11, Oct. 2016. DOI: 10.1161/CIRCEP.116.004398.

[42] J. Jalife, O. Berenfeld, A. Skanes, and R. Mandapati, “Mechanisms of atrial fibrillation: Mother rotors or multiple daughter wavelets, or both?” *J. Cardiovasc. Electrophysiol.*, vol. 9, no. 8, S2–S12, Aug. 1998.

[43] B. Abdi, “Atrial fibrillation fingerprinting,” PhD dissertation, Fac. of Elect. Eng., Math. Comput. Sci., Delft Univ. of Technol., Delft, The Netherlands, 2021. DOI: 10.4233/uuid:af53215c-69ea-4c18-8761-d5cfd2c6e186.

[44] B. Burstein and S. Nattel, “Atrial fibrosis: Mechanisms and clinical relevance in atrial fibrillation,” *J. Am. Coll. Cardiol.*, vol. 51, no. 8, pp. 802–809, Feb. 2008. DOI: 10.1016/J.JACC.2007.09.064.

[45] T. H. Everett and J. E. Olgin, “Atrial fibrosis and the mechanisms of atrial fibrillation,” *Heart Rhythm*, vol. 4, no. 3, pp. S24–S27, Mar. 2007. DOI: 10.1016/J.HRTHM.2006.12.040.

[46] A. Bajpai, I. Savelieva, and A. J. Camm, “Treatment of atrial fibrillation,” *Br. Med. Bull.*, vol. 88, no. 1, pp. 75–94, Dec. 2008. DOI: 10.1093/BMB/LDN046.

[47] M. Brignole *et al.*, “Assessment of atrioventricular junction ablation and DDDR mode-switching pacemaker versus pharmacological treatment in patients with severely symptomatic paroxysmal atrial fibrillation,” *Circulation*, vol. 96, no. 8, pp. 2617–2624, Oct. 1997. DOI: 10.1161/01.CIR.96.8.2617.

[48] H. Kottkamp *et al.*, “Specific linear left atrial lesions in atrial fibrillation: Intraoperative radiofrequency ablation using minimally invasive surgical techniques,” *J. Am. Coll. Cardiol.*, vol. 40, no. 3, pp. 475–480, Aug. 2002. DOI: 10.1016/S0735-1097(02)01993-9.

[49] T. Ashihara *et al.*, “The role of fibroblasts in complex fractionated electrograms during persistent/permanent atrial fibrillation,” *Circ. Res.*, vol. 110, no. 2, pp. 275–284, Jan. 2012. DOI: 10.1161/CIRCRESAHA.111.255026.

[50] I. Nault *et al.*, “Drugs vs. ablation for the treatment of atrial fibrillation: The evidence supporting catheter ablation,” *Eur. Heart J.*, vol. 31, no. 9, pp. 1046–1054, May 2010. DOI: 10.1093/EURHEARTJ/EHQ079.

[51] M. S. Guillem *et al.*, “Noninvasive mapping of human atrial fibrillation,” *J. Cardiovasc. Electrophysiol.*, vol. 20, no. 5, pp. 507–513, May 2009. DOI: 10.1111/j.1540-8167.2008.01356.x.

[52] J. J. Mastrototaro, H. Z. Massoud, T. C. Pilkington, and R. E. Ideker, “Rigid and flexible thin-film multielectrode arrays for transmural cardiac recording,” *IEEE Trans. Biomed. Eng.*, vol. 39, no. 3, pp. 271–279, Mar. 1992. DOI: 10.1109/10.125012.

[53] S. M. Narayan, D. E. Krummen, K. Shivkumar, P. Clopton, W. J. Rappel, and J. M. Miller, “Treatment of atrial fibrillation by the ablation of localized sources: CONFIRM (Conventional Ablation for Atrial Fibrillation with or Without Focal Impulse and Rotor Modulation) trial,” *J. Am. Coll. Cardiol.*, vol. 60, no. 7, pp. 628–636, Aug. 2012. DOI: 10.1016/J.JACC.2012.05.022.

[54] R. Starreveld *et al.*, “Atrial fibrillation fingerprinting; spotting bio-electrical markers to early recognize atrial fibrillation by the use of a bottom-up approach (AFFIP): Rationale and design,” *Clin. Cardiol.*, vol. 43, no. 6, pp. 546–552, Jun. 2020. DOI: 10.1002/CLC.23370.

[55] B. Abdi, R. C. Hendriks, A.-J. van der Veen, and N. M. S. de Groot, “Ventricular activity signal removal in atrial electrograms of atrial fibrillation,” in *Proc. 12th Int. Jt. Conf. Biomed. Eng. Syst. Technol. (BIOSTEC 2019)*, vol. 4, Prague, Czech Republic, Feb. 22–24, 2019, pp. 179–184. DOI: 10.5220/0007388901790184.

[56] B. M. Steinhaus, “Estimating cardiac transmembrane activation and recovery times from unipolar and bipolar extracellular electrograms: A simulation study,” *Circ. Res.*, vol. 64, no. 3, pp. 449–462, Mar. 1989. DOI: 10.1161/01.RES.64.3.449.

[57] M. Beheshti *et al.*, “Determinants of atrial bipolar voltage: Inter electrode distance and wavefront angle,” *Comput. Biol. Med.*, vol. 102, pp. 449–457, Nov. 2018. DOI: 10.1016/J.COMPBIOMED.2018.07.011.

[58] S. Gaeta, T. D. Bahnson, and C. Henriquez, “Mechanism and magnitude of bipolar electrogram directional sensitivity: Characterizing underlying determinants of bipolar amplitude,” *Heart Rhythm*, vol. 17, no. 5, pp. 777–785, May 2020. DOI: 10.1016/J.HRTHM.2019.12.010.

[59] M. Sun, E. Isufi, N. M. S. de Groot, and R. C. Hendriks, “A graph signal processing framework for atrial activity extraction,” in *27th Eur. Signal Process. Conf.*, A Coruña, Spain, Sep. 2–6, 2019. DOI: 10.23919/EUSIPCO.2019.8902778.

[60] T. Moree, “Estimating atrial activity in epicardial electrograms: A beamforming perspective,” MSc thesis, Fac. of Elect. Eng., Math. Comput. Sci., Delft Univ. of Technol., Delft, The Netherlands, 2022. [Online]. Available: http://resolver.tudelft.nl/uuid:b00f0e3d-89d1-4327-8b1d-4b7d6076f225.

[61] C. Kik, E. M. J. P. Mouws, J. J. C. Bogers, and N. M. S. de Groot, “Intra-operative mapping of the atria: The first step towards individualization of atrial fibrillation therapy?” *Expert Rev. Cardiovasc. Ther.*, vol. 15, no. 7, pp. 537–545, Jul. 2017. DOI: 10.1080/14779072.2017.1340156.

[62] M. S. Spach, R. C. Barr, G. A. Serwer, J. M. Kootsey, and E. A. Johnson, “Extracellular potentials related to intracellular action potentials in the dog Purkinje system,” *Circ. Res.*, vol. 30, no. 5, pp. 505–519, May 1972. DOI: 10.1161/01.RES.30.5.505.

[63] M. S. Spach and J. M. Kootsey, “Relating the sodium current and conductance to the shape of transmembrane and extracellular potentials by simulation: Effects of propagation boundaries,” *IEEE Trans. Biomed. Eng.*, vol. BME-32, no. 10, pp. 743–755, Oct. 1985. DOI: 10.1109/TBME.1985.325489.

[64] B. B. Punske *et al.*, “Spatial methods of epicardial activation time determination in normal hearts,” *Ann. Biomed. Eng.*, vol. 31, no. 7, pp. 781–792, Jul. 2003. DOI: 10.1114/1.1581877.

[65] R. Coronel, F. J. Wilms-Schopman, J. R. de Groot, M. J. Janse, R. J. L. van Capelle, and J. M. T. de Bakker, “Laplacian electrograms and the interpretation of complex ventricular activation patterns during ventricular fibrillation,” *J. Cardiovasc. Electrophysiol.*, vol. 11, no. 10, pp. 1119–1128, Oct. 2000. DOI: 10.1111/J.1540-8167.2000.TB01758.X.

[66] R. C. Cabot, “A note on the application of the Hilbert transform to time delay estimation,” *IEEE Trans. Acoust., Speech, Signal Process.*, vol. 29, no. 3, pp. 607–609, Jun. 1981. DOI: 10.1109/TASSP.1981.1163564.

[67] S. M. Shors, A. V. Sahakian, H. J. Sih, and S. Swiryn, “A method for determining high-resolution activation time delays in unipolar cardiac mapping,” *IEEE Trans. Biomed. Eng.*, vol. 43, no. 12, pp. 1192–1196, Dec. 1996. DOI: 10.1109/10.544343.

[68] F. X. Witkowski, K. M. Kavanagh, P. A. Penkoske, and R. Plonsey, “In vivo estimation of cardiac transmembrane current,” *Circ. Res.*, vol. 72, no. 2, pp. 424–439, Feb. 1993. DOI: 10.1161/01.RES.72.2.424.

[69] W. S. Ellis, S. J. Eisenberg, D. M. Auslander, M. W. Dae, A. Zakhor, and M. D. Lesh, “Deconvolution: A novel signal processing approach for determining activation time from fractionated electrograms and detecting infarcted tissue,” *Circulation*, vol. 94, no. 10, pp. 2633–2640, Nov. 1996. DOI: 10.1161/01.CIR.94.10.2633.

[70] I. Chouvarda, N. Maglaveras, J. M. T. de Bakker, F. J. L. van Capelle, and C. Pappas, “Deconvolution and wavelet-based methods for membrane current estimation from simulated fractionated electrograms,” *IEEE Trans. Biomed. Eng.*, vol. 48, no. 3, pp. 294–301, Mar. 2001. DOI: 10.1109/10.914792.

[71] A. Cohen and J. Kovačević, “Wavelets: The mathematical background,” *Proc. IEEE*, vol. 84, no. 4, pp. 514–522, Apr. 1996. DOI: 10.1109/5.488697.

[72] B. Abdi, R. C. Hendriks, A.-J. van der Veen, and N. M. S. de Groot, “A compact matrix model for atrial electrograms for tissue conductivity estimation,” *Comput. Biol. Med.*, vol. 107, pp. 284–291, Apr. 2019. DOI: 10.1016/j.compbiomed.2019.02.012.

[73] R. P. M. Houben, N. M. S. de Groot, F. W. Lindemans, and M. A. Allessie, “Automatic mapping of human atrial fibrillation by template matching,” *Heart Rhythm*, vol. 3, no. 10, pp. 1221–1228, Oct. 2006. DOI: 10.1016/J.HRTHM.2006.06.009.

[74] R. P. M. Houben and M. A. Allessie, “Processing of intracardiac electrograms in atrial fibrillation: Diagnosis of electropathological substrate of AF,” *IEEE Eng. Med. Biol. Mag.*, vol. 25, no. 6, pp. 40–51, Nov.–Dec. 2006. DOI: 10.1109/EMB-M.2006.250507.

[75] E. F. Treo, D. O. Cervantes, and E. J. Ciaccio, “Automated detection and mapping of electrical activation when electrogram morphology is complex,” *Biomed. Signal Process. Control*, vol. 8, no. 1, pp. 41–49, Jan. 2013. DOI: 10.1016/J.BSPC.2012.04.006.

[76] B. Kölling, “Atrial activation time estimation using cross-correlation between higher order neighboring electrodes in epicardial electrograms,” MSc thesis, Fac. of Elect. Eng., Math. Comput. Sci., Delft Univ. of Technol., Delft, The Netherlands, 2019. [Online]. Available: http://resolver.tudelft.nl/uuid:2a460639-d762-40c4-bb21-cf4cbffe0a6b.

[77] B. Abdi, R. C. Hendriks, A.-J. van der Veen, and N. M.S. de Groot, “Local activation time annotation in atrial electrogram arrays using deconvolution,” in *Comput. Cardiol. 2019*, vol. 45, Singapore, Sep. 8–11, 2019, pp. 2019–2022. DOI: 10.22489/cinc.2019.178.

[78] R. Plonsey and R. C. Barr, *Bioelectricity: A Quantitative Approach*, 3rd ed. Cham, Switzerland: Springer, 2007, ISBN: 978-0-387-48864-6.

[79] S. P. Boyd and L. Vandenberghe, *Convex Optimization*. Cambridge, U.K.: Cambridge Univ. Press, 2004, ISBN: 978-0-521-83378-3.

[80] C. Godsil and G. F. Royle, *Algebraic Graph Theory*, 1st ed. New York, NY, USA: Springer-Verlag, 2001. DOI: 10.1007/978-1-4613-0163-9.

[81] R. Penrose, “A generalized inverse for matrices,” *Math. Proc. Cambridge Philos. Soc.*, vol. 51, no. 3, pp. 406–413, Jul. 1955. DOI: 10.1017/S0305004100030401.

[82] M. A. Allessie *et al.*, “Electropathological substrate of longstanding persistent atrial fibrillation in patients with structural heart disease: Longitudinal dissociation,” *Circ. Arrhythmia Electrophysiol.*, vol. 3, no. 6, pp. 606–615, Dec. 2010. DOI: 10.1161/CIRCEP.109.910125.

[83] E. Vigmond, A. Pashaei, S. Amraoui, H. Cochet, and M. Hassaguerre, “Percolation as a mechanism to explain atrial fractionated electrograms and reentry in a fibrosis model based on imaging data,” *Heart Rhythm*, vol. 13, no. 7, pp. 1536–1543, Jul. 2016. DOI: 10.1016/J.HRTHM.2016.03.019.

[84] V. Jacquemet and C. S. Henriquez, “Genesis of complex fractionated atrial electrograms in zones of slow conduction: A computer model of microfibrosis,” *Heart Rhythm*, vol. 6, no. 6, pp. 803–810, Jun. 2009. DOI: 10.1016/J.HRTHM.2009.02.026.

[85] J. M. Rogers, M. Usui, B. H. KenKnight, R. E. Ideker, and W. M. Smith, “Recurrent wavefront morphologies: A method for quantifying the complexity of epicardial activation patterns,” *Ann. Biomed. Eng.*, vol. 25, no. 5, pp. 761–768, Sep. 1997. DOI: 10.1007/BF02684160.

[86] J. M. Rogers, M. Usui, B. H. KenKnight, R. E. Ideker, and W. M. Smith, “A quantitative framework for analyzing epicardial activation patterns during ventricular fibrillation,” *Ann. Biomed. Eng.*, vol. 25, no. 5, pp. 749–760, Sep. 1997. DOI: 10.1007/BF02684159.

Abbreviations

AF atrial fibrillation

AM activation map

AP action potential

AV atrioventricular

BB Bachmann's bundle

CAS Circuits and Systems

CV conduction velocity

CVD cardiovascular disease

ECG electrocardiogram

EGM electrogram

ETV Electrotechnische Vereeniging

ICV inferior caval vein

LA left atrium

LAA left atrial appendage

LAT local activation time

NCC normalized cross-correlation

NDCC normalized cross-correlation of the time derivative

PV pulmonary vein

PVI pulmonary-vein isolation

RA right atrium

RAA right atrial appendage

RMSE root-mean-square error

SA sinoatrial

SCV superior caval vein

SD steepest deflection

SNR signal-to-noise ratio

SR sinus rhythm

SVD singular-value decomposition

Symbols

$\hat{x}$ estimate of variable x

x scalar

$\mathbf{x}$ column vector

$\mathbf{X}$ matrix

$\mathbf{x}^\mathsf{T}$, $\mathbf{X}^\mathsf{T}$ transpose of a vector or a matrix

$\mathbf{X}^{-1}$ inverse of the non-singular matrix $\mathbf{X}$

$\mathbf{X}^\dagger$ pseudo-inverse of the matrix $\mathbf{X}$

$\mathbf{X}^p$ $\underbrace{\mathbf{X}\mathbf{X}\cdots\mathbf{X}}_{p}$

$[\mathbf{X}]_{i,j}$ element of matrix $\mathbf{X}$ at row i and column j

$\mathrm{rank}(\mathbf{X})$ rank of the matrix $\mathbf{X}$, i.e., dimension of its column space

$\mathrm{diag}(\mathbf{x})$ diagonal matrix with the vector $\mathbf{x}$ as its main diagonal

$\mathrm{diag}(\mathbf{X})$ vector containing the diagonal elements of the matrix $\mathbf{X}$

$\mathbf{I}$ identity matrix of appropriate size

$y(t)$ quantity indexed by the continuous variable t

$y[t]$ quantity indexed by the discrete variable t

y' first-order time derivative of y

$\boldsymbol{\nabla}$ nabla operator

$\boldsymbol{\nabla} \cdot \mathbf{E}$ divergence of the vector-valued function $\mathbf{E}$

$\boldsymbol{\nabla} E$ gradient of the scalar-valued function E

$\| \cdot \|$ norm

$\| \cdot \|_1$ l_1-norm

$\| \cdot \|_2$ l_2-norm

$\mathbb{R}$ set of real numbers

$|E|$ cardinality of the set E

$\mathbb{E}[\cdot]$ expected-value operator

$\mathrm{Cov}(\cdot)$ covariance of a multivariate random variable

$\mathcal{N}(\boldsymbol{\mu}, \mathbf{C})$ multivariate Gaussian distribution with mean $\boldsymbol{\mu}$ and covariance $\mathbf{C}$